Towards Reliable UAV-Enabled Positioning in Mountainous Environments: System Design and Preliminary Results

Towards Reliable UAV-Enabled Positioning in Mountainous Environments: System Design and Preliminary Results

Zijie Wang, Rongke Liu, *Senior Member, IEEE,* Qirui Liu, Lincong Han, John S. Thompson, *Fellow, IEEE,* Yun Lin, *Member, IEEE,* and Weiqing Mu

***Abstract*—Reliable positioning services are extremely important for users in mountainous environments. However, in such environments, the service reliability of conventional wireless positioning technologies is often disappointing due to frequent non-line-of-sight (NLoS) propagation and poor geometry of available anchor nodes. Hence, we propose a unmanned aerial vehicle (UAV)-enabled positioning system that utilizes UAV's mobility to overcome the above challenges. In this article, we first analyze and model the major causes of service failures in the proposed system. In particular, a geometry-based NLoS probability model is established based on the digital elevation models (DEM) of realistic terrain for reliability analysis. Subsequently, we propose a reliability prediction method and derive the corresponding metric to evaluate the system's ability to provide reliable positioning services. Moreover, we also develop a voting-based method for the further enhancement of service reliability. Monte-Carlo simulations show that in mountainous environments, the proposed reliability prediction method could achieve a prediction accuracy that is at least 36.8% higher than that of the existing technique. In addition, in the experiments conducted in two typical valley scenarios, the proposed reliability enhancement method improves the service reliability of the proposed system by 23% and 29%, respectively. These numerical results demonstrate the strong potential of the proposed system and methods for reliable positioning.**

***Index Terms*—Unmanned aerial vehicle (UAV), UAV-enabled positioning, reliability prediction, reliability enhancement, mountainous environments.**

I. Introduction

A. Motivation

MOTIVATED by the explosive growth of applications that require or benefit from location information, positioning technologies are playing an increasingly important role in our everyday lives [1]. Both the Narrowband Internet of Things (NB-IoT) and the fifth generation (5G) wireless network have considered positioning as an enabling technology and essential service in 3rd Generation Partnership Project (3GPP) Release 14 and Release 16, respectively [2], [3]. A mountainous environment is one of the typical deployment scenarios of 5G and NB-IoT [4], [5], in which the positioning service is also extremely important. Different from plain or city environments, the terrain in mountainous environments is complex and highly variable, so that large position errors caused by faults or anomalies may result in economic losses or even loss of life. Thus, the reliability of positioning services should be a major concern in mountainous environments.

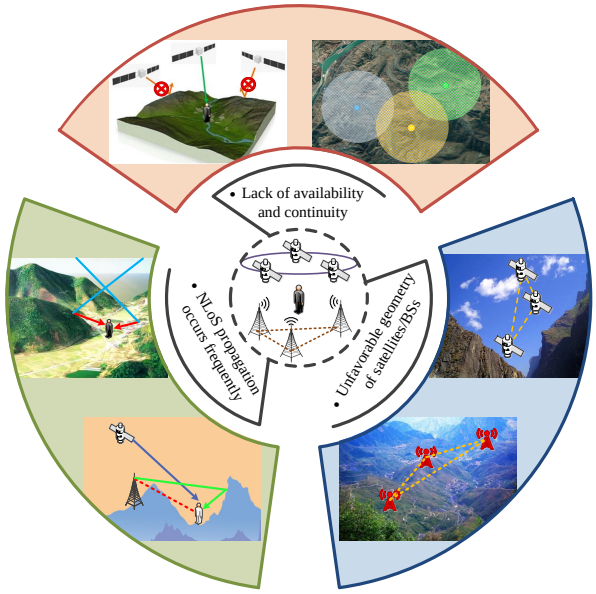

Fig. 1. Limitations of existing positioning technologies in mountainous environments.

Thanks to the continuous development of consumer electronics industries over the past two decades, almost every smartphone or wearable device today is equipped with a global navigation satellite system (GNSS) receiver, which could provide users with satisfactory positioning services in open-sky environments [6]. Besides, since 3GPP Release 9, terrestrial cellular networks have supported a variety of cellular-based positioning technologies like the observed time difference of arrival (OTDoA) positioning [7]. On account of this, mobile phone users could use the cellular network to locate themselves even in some GNSS degraded environments like dense urban and indoors [8], [9]. However, although GNSS systems

This work was supported by the Beijing Municipal Science and Technology Project (Z181100003218008).

Z. Wang, R. Liu, Q. Liu and L. Han are with the School of Electronic and Information Engineering, Beihang University, Beijing 100191, China (e-mail: wangmajie@buaa.edu.cn; rongke_liu@buaa.edu.cn).

J. S. Thompson is with the Institute for Digital Communications, School of Engineering, University of Edinburgh, King's Buildings, Edinburgh, EH9 3JL, U.K. (e-mail: john.thompson@ed.ac.uk).

Y. Lin is with the Key Laboratory of Advanced Marine Communication and Information Technology, College of Information and Communication Engineering, Harbin Engineering University, Harbin 150001, China.

W. Mu is with China Research Institute of Radiowave Propagation, Qingdao 266107, China (e-mail: weiqing0017@163.com).

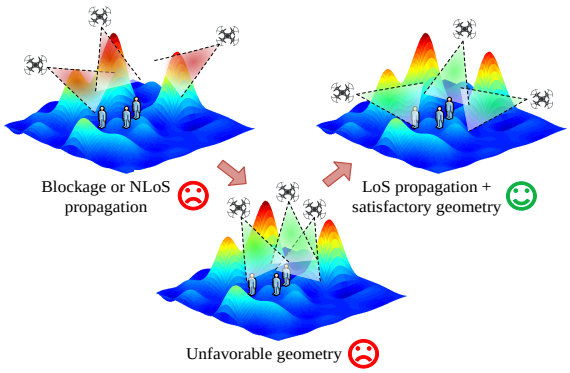

Fig. 2. Advantages of UAV-enabled positioning in mountainous environments.

and cellular-based positioning technologies have been fruitfully applied in our daily lives, their performance in mountainous environments may be somewhat disappointing. As shown in Fig. 1, for the widely used GNSS positioning technology, the weak signals are frequently blocked by rugged terrain like peaks and ridges, resulting in very limited availability and continuity of service [10], [11]. Moreover, the signal detected by the receiver may not be the desired direct (LoS) signal from the satellite, but a reflected signal from the mountains [12]. This phenomenon, known as NLoS propagation, will severely degrade the performance of the positioning service, causing errors of several meters to hundreds of meters. Another challenge for GNSS users in mountainous environments is the unfavorable geometry of the satellites in-view [13]. For instance, the satellites available to the user in a valley are mainly in the direction along the valley, since radio signals going across the valley are very likely to be blocked by the terrain. This poor satellite geometry leads to unsatisfactory accuracy and reliability in the across-valley direction. Cellular-based positioning has the same limitations as GNSS [14], including insufficient numbers of available base stations (BSs), unfavorable geometry of BSs, and NLoS propagation. To make matters worse, since the elevation angles of terrestrial BSs are generally much lower than those of GNSS satellites, cellular signals are more likely to experience NLoS propagation than GNSS signals [15]. It is therefore unwise to expect cellular networks to perform better than GNSS systems. To the best of our knowledge, the implementation of reliable positioning in mountainous environments remains an open question.

Due to their high maneuverability and flexible deployment, UAVs have attracted a lot of interest in recent years [16]. In the field of communication, a UAV could act as an aerial BS to provide network connectivity for ground users [17], or coordinate with other UAVs to form ad hoc networks and share information with each other [18], [19]. Moreover, as the reliability of their own state estimation and control continues to improve [20], [21], UAVs are capable of performing tasks with requirements for high reliability like reliable video transmission [22]. Except being used for communication, UAVs are also suitable for providing positioning services, especially in terms of reliable positioning. Utilizing high-performance airborne navigation equipment like real-time kinematic (RTK) receivers, UAVs have the ability to precisely determine their own locations in real time, enabling them to be employed as aerial anchor nodes [23]. As shown in Fig. 2, compared with satellites operating in fixed orbits or BSs fixed on the ground, UAV platforms have their unique advantages. First, UAVs are capable of flying to places where the channel conditions to users are good [24]. Therefore, through the optimization of the flight trajectory or deployment strategy, UAV platforms can provide users with a sufficient number of measurements, and effectively reduce the probability of NLoS propagation. Moreover, if the geometry of anchor nodes is also taken into account in the design of the UAV trajectory [25], the problem of unfavorable geometry common in GNSS and cellular-based positioning could be largely avoided. From the above analysis, it can be concluded that the UAV-enabled positioning system is a good choice for providing reliable positioning services in mountainous environments.

B. Related Work

UAV-enabled positioning that employs UAV platforms to provide positioning services is not a new concept. In fact, some studies pointed out more than a decade ago that UAVs and many other types of platform have the potential to be used as mobile anchor nodes to determine users' locations [26], [27]. In the past few years, several prototypes of UAV-enabled positioning systems have been developed and tested in the research community, such as HAWK (UMass Lowell) [28] and GuideLoc (NWU, China) [29]. Most of these existing systems adopt range-free localization approaches, which limit their ability to provide accurate and reliable positioning services. Moreover, their positioning performance is only tested in ideal environments like a sports field or campus, which cannot effectively reflect the accuracy and reliability of positioning services in all scenarios. With the development of airborne sensors, many recent studies began to use range-based localization approaches, so as to make their systems suitable for missions requiring high positioning accuracy. Sallouha *et al*. [30], [31] proposed a system that uses UAVs and the received signal strength (RSS) technique to locate terrestrial nodes, and analyzed the influences of UAV altitude and trajectory on positioning performance. In [25], a UAV platform was employed to assist the terrestrial IoT network in energy-efficient data collection and three-dimensional (3-D) TDoA positioning. These two studies mainly focused on the improvement of positioning accuracy, and used the Cramér-Rao lower bound (CRLB) to evaluate the system performance. The CRLB is a useful evaluation metric for location estimation under fault-free conditions as it defines a lower limit for the variance of any unbiased estimator. However, the CRLB cannot reflect the positioning accuracy and reliability under faulty conditions where most location estimators are no longer unbiased. Table I summarizes the above-mentioned systems and their characteristics.

Unlike UAV-enabled positioning, the GNSS community has paid a great deal of attention to reliability issues. The detection of service failures caused by faults or anomalies is one of the most basic capabilities for reliable positioning systems. In GNSSs, Receiver Autonomous Integrity Monitoring (RAIM) is

TABLE I
SUMMARY OF EXISTING UAV-ENABLED POSITIONING SYSTEMS AND COMPARISON WITH THE PROPOSED SYSTEM

Ref.	Objective	Localization Approach	Positioning Performance Metric	Test Environment	Consider NLoS Propagation	Ability to Detect Failure
[25]	Positioning accuracy & energy consumption	Range-based (OTDoA)	CRLB (m^2)	Unspecified	No	No
[26]	Positioning accuracy	Range-free (perpendicular bisector of chord)	Average location error (m)	Outdoor open field	Unspecified	No
[28]	Positioning accuracy & flight distance	Range-free (waypoiint with strongest signal)	Average location error (m)	Track field	Unspecified	No
[29]	Positioning accuracy & time consumption	Range-free (direction with strongest signal)	Average location error (m)	Football field	Unspecified	No
[30]	Positioning accuracy	Range-based (RSS)	CRLB (m^2)	Urban	Yes	No
[31]	Positioning accuracy & energy consumption	Range-based (RSS)	CRLB (m^2)	Urban	Yes	No
Proposed system	Service reliability	Range-based (TWR)	Minimum detectable error (m)	Mountainous environments	Yes	Yes

TABLE II
SUMMARY OF RAIM METHODS AND COMPARISON WITH THE PROPOSED RELIABILITY PREDICTION METHOD

Ref.	Target applications	Detection method	Handling of multiple faults	Types of faults considered	Prior probabilities of faults	Offline reliability prediction
[32]	GNSS applications (civil aviation)	LS residuals method	No	Satellite faults	Preset constants	No
[33]	GNSS applications (civil aviation)	Maximum SS method	No	Satellite faults	Preset constants	No
[34]	GNSS applications (civil aviation)	Multiple hypothesis LS residuals method	Yes	Satellite faults	Preset constants	No
[35]	GNSS applications (civil aviation)	Multiple hypothesis SS method	Yes	Satellite faults	Preset constants	No
Proposed method	UAV-enabled positioning	Multiple hypothesis LS residuals method	Yes	UAV internal faults & NLoS propagation	Calculated with DEM data of realistic terrains	Yes

a well-known technique used for detecting large position errors [32]. Since the late 1980s, many different RAIM methods have been developed and successfully applied in the aviation domain, such as the least squares (LS) residuals method and the solution separation (SS) method [32], [33]. It should be noted that these classic RAIM methods are based on the single-fault assumption, which is not true for UAV-enabled positioning in mountainous environments. First, there is no doubt that the failure rates of low-cost airborne sensors are much higher than those of GNSS satellites. Besides, frequent NLoS propagation also increases the probability of multiple simultaneous faults. In [34], [35], the LS and SS RAIM were extended to multiple-fault conditions. However, despite being one of the major causes of service failures in mountainous environments, the NLoS propagation was not considered in these studies [36]. In addition, these methods are all online failure detection methods [32]–[35], which means that they can only evaluate the reliability of positioning services when the visibility of each anchor node is already known. Nevertheless, for a UAV-enabled positioning system, it is impossible to determine whether the UAV at a certain location is visible to the user before the mission starts. Then, the above online failure detection methods cannot be used for reliability prediction that is essential for UAV-enabled positioning. Thus, existing failure detection methods represented by the RAIM technique cannot be directly applied to UAV-enabled positioning, but they can still provide valuable inspiration for the design of our reliable positioning system. Table II summarizes the existing failure detection methods and their characteristics.

Reliability enhancement refers to a class of measures that need to be taken when the predicted or evaluated reliability of a positioning system does not meet the requirements. Since we have not yet found any reliability enhancement methods developed specifically for UAV-enabled positioning, the research works discussed in this paragraph mainly focus on the reliability enhancement in GNSS positioning. In GNSSs, there are some existing enhancement methods that have the ability to improve the reliability of positioning services. For example, Meng *et al*. [37], [38] pointed out that the positioning reliability in GNSS could be improved by appropriately selecting satellites from multiple constellations. For the well-known ground-based augmentation system (GBAS), the reliability of GNSS positioning is enhanced by utilizing a large amount of ground stations to monitor GNSS signals and broadcast the monitoring information to users [39], [40]. Similarly, the satellite-based augmentation system (SBAS) also achieves the

TABLE III
SUMMARY OF EXISTING RELIABILITY ENHANCEMENT METHODS AND COMPARISON WITH THE PROPOSED METHOD

Ref.	Measures for enhancing service reliability	Requirements for additional facilities	Cost	Flexibility
[37], [38]	Appropriate selection of satellites from multiple GNSS constellations	Additional satellite constellations	High	Low
[39], [40] (GBAS)	Signal monitoring and information broadcasting carried out by ground stations	Ground stations	High	Low
[41], [42] (SABS)	Signal monitoring performed by ground stations & Information broadcasting performed by satellites	Ground stations & additional satellites	High	Low
Proposed method	Appropriate adjustment of the locations where the UAV provides positioning services	None	Low	High

goal of reliability enhancement by monitoring GNSS signals, except that the data broadcasting is performed by satellites to cover a wider area [41], [42]. It can be seen from the above analysis that the application of these existing reliability enhancement methods commonly requires additional facilities (satellites, ground stations, etc.), which are costly and inflexible. If we directly apply these existing methods to UAV-enabled positioning, it will undoubtedly be a waste of UAVs' high maneuverability and flexibility. Therefore, it is necessary to develop novel reliability enhancement methods based on the characteristics and advantages of UAV-enabled positioning. Table III summarizes the existing reliability enhancement methods and their characteristics.

C. Research Questions, Contributions and Novelty

As discussed in the above subsection, the drawback of the existing UAV-enabled positioning systems is that they mainly focus on accuracy rather than service reliability, making them unsuitable for providing positioning services in mountainous environments. However, the existing failure detection methods widely used in GNSSs cannot be directly applied to UAV-enabled positioning due to the lack of the abilities to handle NLoS propagation and perform offline reliability prediction. Moreover, the existing reliability enhancement methods commonly require the construction of additional facilities like ground stations, which is impractical for UAV systems deployed in complex terrains.

As mentioned at the beginning of this article, our aim is to design a UAV-enabled positioning system to provide reliable services in mountainous environments. Therefore, the drawbacks of the existing systems and methods are exactly the research questions to be studied in this article. Specifically, we mainly focus on the following questions:

1) *How to detect service failures caused by NLoS propagation?* The prior probabilities of faults are essential for failure detection, because they directly affect the setting of decision thresholds. However, unlike those "internal faults" in airborne sensors or user equipment, the prior probabilities of NLoS propagation are unknown and closely related to the surrounding environments. This characteristic makes it difficult to effectively detect service failures caused by NLoS propagation with failure detection methods.
2) *How to predict the service reliability before the UAV takes off?* The visibility of the UAV at a certain location to the user cannot be fully determined before the UAV takes off and establishes the wireless link. Thus, the service reliability has to be predicted without knowing which observation event will happen, which is obviously a challenge for the calculation of the minimum detectable error.
3) *How to enhance the service reliability without additional facilities?* The complex terrains in mountainous environments are unsuitable for the construction of ground stations and other facilities. Without the help of additional facilities, the reliability enhancement in UAV-enabled positioning can only be achieved by utilizing the high mobility and flexible deployment of the UAV itself, which has not been studied in previous research.

Through the analysis and study of the above research questions, we propose a novel UAV-enabled positioning system for mountainous environments. Different from existing systems, the proposed system focuses on the reliability of positioning services, which is defined as the minimum position error that can be effectively detected during the positioning process. The main contributions of this article are the design, modeling, application and evaluation of the proposed system. Specifically, we first design the system structure and the corresponding operation scheme according to the application requirements. Then, the model of service failures in the proposed system caused by two types of faults, namely the internal faults and NLoS propagation, is established with the DEM data of realistic terrains. Based on the established failure model, we propose a reliability prediction method that could accurately evaluate the reliability of positioning services before the UAV takes off and derive the corresponding metric. In addition, we also conduct a preliminary study on reliability enhancement, and propose a voting-based cause analysis method to provide guidance for the adjustments of UAV's locations. Finally, the effectiveness, applicability and robustness of the proposed system and methods in mountainous environments are carefully evaluated and verified through several simulation experiments.

Compared with the existing systems and methods, the main novelty of the proposed system is that we introduce the DEM data of realistic terrains into UAV-enabled positioning, and develop novel reliability prediction and enhancement methods based on it. The DEM data enables us to predict the signal blockage and NLoS propagation caused by complex terrains, which provides the basis for the realization of offline reliability prediction and enhancement in mountainous environments.

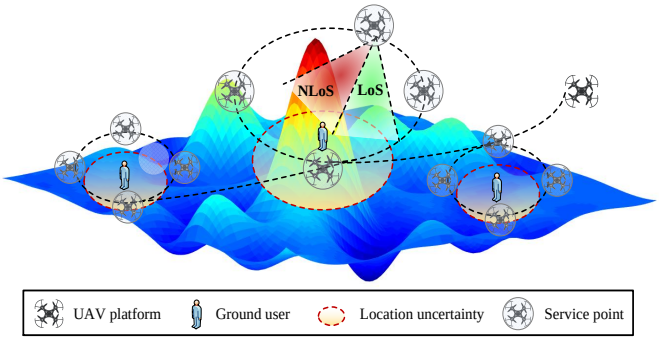

Fig. 3. Proposed UAV-enabled positioning system.

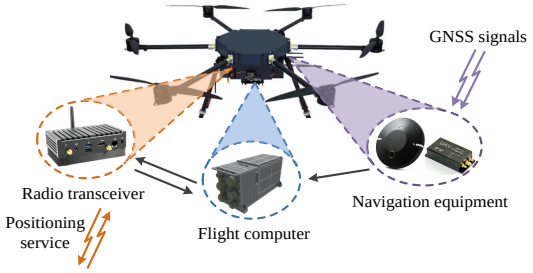

Fig. 4. Main components of the UAV platform.

Specifically, our solutions to the existing systems' drawbacks and the above-mentioned research questions are summarized as follows.

1) *Detection of service failures caused by NLoS propagation*: Based on the DEM data of realistic terrains, we develop a geometry-based stochastic model that can be used to calculate the prior probabilities of NLoS propagation. Then, the NLoS propagation caused by complex terrains in mountainous environments can also be treated as a type of faults and can be effectively detected by failure detection methods.
2) *Realization of offline reliability prediction*: With the proposed geometry-based stochastic model, we can also calculate the prior probabilities of signal blockage. Thus, although it is still impossible to determine which observation event will happen, the prior probabilities of each event can be obtained. Then, we analyze each possible observation event and calculate the corresponding service reliability (minimum detectable error) according to its prior probability. The worst service reliability in all observation events is taken as the result of offline reliability prediction.
3) *Realization of reliability enhancement with UAV's mobility*: Unlike existing enhancement methods that require addition facilities, the proposed system improves the reliability of positioning services by appropriately adjusting the deployment locations of the UAV platform. We propose a voting-based method to analyze the causes of unsatisfactory reliability. Based on the analysis results and DEM data, we adjust the UAV's locations to obtain better service reliability.

To illustrate the novelty and advantages of the proposed system, we compare it with existing systems and methods in Table I-III. To the best of our knowledge, this work is the first to study the service reliability of UAV-enabled positioning systems in mountainous environments.

D. Organization and Notations

This article is organized as follows. The structure of the proposed system and mathematical models for localization are given in Section II. In Section III, the proposed reliability prediction method and its corresponding metric are derived. Section IV introduces our preliminary study on reliability enhancement. Section V provides numerical results to demonstrate the potential of our system and the effectiveness of the proposed methods. In Section VI, we analyze the issues that could threaten the validity of our system and methods. Section VII concludes this article. Finally, in Section VIII, the future direction of this work is introduced.

The notations are summarized as follows. Column vectors and matrices are denoted by lowercase and uppercase boldface letters ($\mathbf{a}$ and $\mathbf{A}$), respectively. The superscript T indicates the transpose operation ($\mathbf{A}^T$) and superscript -1 indicates matrix inverse ($\mathbf{A}^{-1}$). $\langle\cdot\rangle$ denotes the integer rounding operation.

II. System Design

As shown in Fig. 3, we consider a scenario consisting of a low-altitude UAV platform and multiple ground users who are scattered over a typical mountainous environment. The users could be hikers or injured people who are trapped and awaiting rescue, and our first priority is to determine their locations. Each user has a barometer embedded in his/her smartphone that can provide accurate altitude information. However, in such an environment, users cannot use the GNSS systems or cellular networks to obtain their horizontal locations due to the lack of service availability and reliability [10]–[12]. Therefore, we expect the UAV platform to undertake the task of locating ground users. Fig. 4 shows the three main types of payloads carried on the UAV platform: 1) the navigation equipment used to determine the real-time precise location of the UAV itself; 2) a radio transceiver for transmitting and receiving positioning reference signal (PRS); and 3) a flight computer for flight control and location estimation. These payloads enable the UAV platform to be employed as an aerial anchor node to provide positioning services for ground users.

The UAV platform flies at a fixed altitude h_B. During the mission, the UAV flies from the initial location to the final location along a specific trajectory under control of the flight computer. When passing through the area where a ground user is located, the UAV will hover at multiple carefully selected service points (SPs) and perform two-way ranging (TWR). After all the SPs corresponding to the user have been traversed, its location can be estimated from the obtained range measurements utilizing multilateration algorithms.

In this article, we mainly focus on the reliability prediction and enhancement of the positioning service provided for each user. Besides, we assume that ground users are far apart, so that the UAV platform can only serve one user at each SP. This assumption is reasonable because multiple users

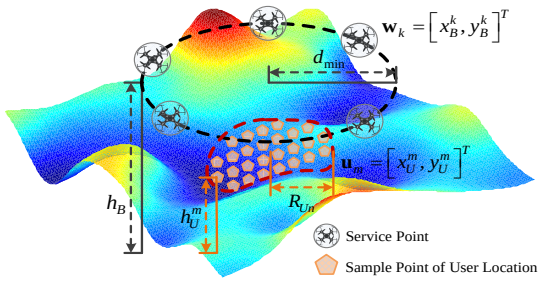

Fig. 5. Scenario of single user.

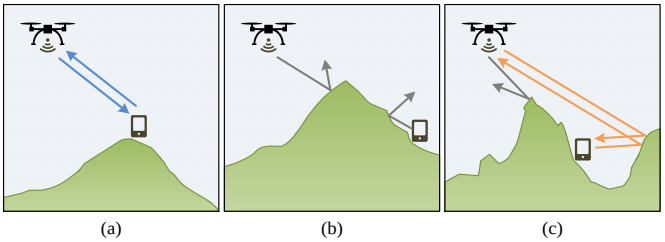

Fig. 6. Three types of propagation conditions in mountainous environments: (a) LoS condition, (b) Blockage condition and (c) NLoS condition.

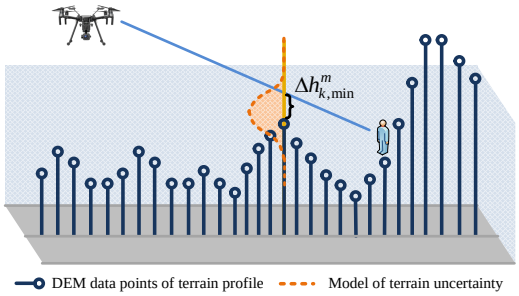

Fig. 7. Probability model of signal propagation condition.

that are close to each other can be equivalently regarded as one user with larger location uncertainty in practice. Then, the overall scenario described above can be divided into several single-user scenarios, as shown in Fig. 5. The precise location of the user is unknown before the UAV provides the positioning service. However, the location uncertainty area where the user is located can be obtained in advance based on historical information and motion prediction [43]. The boundary of the uncertainty area is indicated by the red dotted line in Fig. 5, and its projection onto the horizontal plane is a circle of radius R_{Un}. For convenience, the location uncertainty area is discretized into M sample points, denoted by the set $\mathcal{M} \triangleq \{1, 2, \cdots, M\}$. The 3-D location of the m-th sample point is denoted by the horizontal coordinate $\mathbf{u}_m = (x_U^m, y_U^m)^T \in \mathbb{R}^{2\times 1}$, $m \in \mathcal{M}$, and the altitude h_U^m. In addition, the prior probability that the user is located at each sample point is assumed to be equal. For each ground user, we set K SPs to provide the positioning service, denoted by the set $\mathcal{K} \triangleq \{1, 2, \cdots, K\}$. The horizontal coordinate of the k-th SP is denoted by $\mathbf{w}_k \triangleq \left(x_B^k, y_B^k\right)^T \in \mathbb{R}^{2\times 1}$, $k \in \mathcal{K}$. It should be noted that there is a minimum distance requirement for the setting of SPs. Specifically, the horizontal distance between a SP and the center of the location uncertainty area should be no less than $d_{\min}$. The reason for this requirement is to ensure that large position errors caused by faults or anomalies will not bring significant changes to the geometry of SPs relative to the user, so that the service reliability could be evaluated or predicted without making assumptions on the values or distributions of unknown faults. Obviously, reducing the horizontal distance will increase the UAV elevation angle, resulting in a smaller probability of signal blockage or NLoS propagation. Thus, in this article, in order to ensure the reliability of the positioning service, SPs will be set on a circle of radius $d_{\min}$, which is indicated by the black dotted line in Fig. 5. In future work, we will consider more general definitions of the SP locations.

The above paragraphs describe the structure, operation scheme and application scenario of the proposed UAV-enabled positioning system. In the following two subsections, we provide some technical details. We first introduce a geometry-based probability model used to characterize the propagation conditions in mountainous environments. Then, the probability model of service failure that is essential for reliability prediction is established.

A. Signal Propagation Model

As shown in Fig. 6, for air-to-ground (A2G) channels in mountainous environments, there are three types of propagation conditions that need to be analyzed: 1) *LoS condition* where a LoS radio path exists between the UAV and the ground user; 2) *Blockage condition* where both the direct (LoS) and reflected signals are blocked by surrounding terrain and cannot be detected by the receiver; and 3) *NLoS condition* where the direct signal is blocked and only reflected signals are received. Among these three conditions, the LoS condition is the most favorable one since it provides the range measurement with the lowest error [44], [45]. The occurrence of the blockage condition will reduce the number of available measurements and thus affect the positioning performance, but it is not a direct cause of service failures. The NLoS condition is always a challenging problem for most range-based positioning systems as it imposes significant bias in both ranging and positioning. It should be noted that the multipath interference that frequently occurs in mountainous environments is not considered in this article, because we believe that existing techniques such as the multipath estimating delay lock loop (MEDLL) are sufficient to mitigate the impacts of multipath [46]. From the above analysis, it can be concluded that these three propagation conditions have distinct effects on positioning services, requiring us to treat them differently. However, the exact propagation condition of an A2G channel cannot be fully determined before the wireless link is established. Thus, in this subsection, we determine the prior probability of each condition.

Different from most existing research that employs distance-based or elevation angle based LoS probability models to characterize the A2G channel [47], [48], in this article, we develop a geometry-based stochastic model based on the DEM of the realistic terrain. Fig. 7 shows the terrain profile between

the *k*-th SP of the UAV platform and the *m*-th sample point of user's location, which is reconstructed using the DEM data. The methods for reconstructing the terrain profile are described in [49]. Assuming that the measurement error in DEM data is negligible and the DEM resolution is extremely high, the LoS condition could be easily identified by checking whether all DEM data points are below the UAV-user LoS (blue solid line). Obviously, this assumption is unrealistic in practice. In fact, the DEM error or so-called "terrain uncertainty" caused by the measurement error and limited resolution is widely considered to be an important factor affecting the performance of DEM-based applications [50], [51], and therefore should be taken into account when analyzing the signal propagation condition [49]. To address this problem, we model the terrain uncertainty as an additive white Gaussian noise n_h (orange dotted line) added to the minimum difference in height $\Delta h^m_{k,\min}$ between DEM data points and the UAV-user LoS.[1] The above model of terrain uncertainty is reasonable in practice, because the Gaussian distribution has been widely used to describe the distribution of vertical uncertainty on the DEM [50], [51]. Then, the actual minimum height difference with the consideration of location uncertainty is given by

$$\Delta\tilde{h}^m_{k,\min} = \Delta h^m_{k,\min} + n_h, \quad n_h \sim \mathcal{N}\left(0, \sigma_h^2\right), \tag{1}$$

where σ_h^2 denotes the variance of terrain uncertainty. The prior probability of LoS condition is defined as the probability that $\Delta\tilde{h}^m_{k,\min}$ is positive, which can be expressed as

$$P^m_{k,LoS} = P\left(\Delta h^m_{k,\min} + n_h > 0\right) = 1 - F_{n_h}\left(-\Delta h^m_{k,\min}\right), \tag{2}$$

where $F_x(t) = \frac{1}{\sigma_x\sqrt{2\pi}}\int_{-\infty}^{t}\exp\left(-\frac{(x-\mu_x)^2}{2\sigma_x^2}\right)dx$ denotes the cumulative distribution function (CDF) of the random variable x, and μ_x is its mean value.

Contrary to the LoS condition, the prior probability that the LoS path does not exist is $P^m_{k,No\_LoS} = 1 - P^m_{k,LoS}$. In the absence of the LoS path, two types of potential propagation conditions still need to be distinguished, namely the blockage condition and the NLoS condition. The basis for distinguishing these two conditions is whether the received reflected signals are strong enough to be detected by the receiver. In this article, we employ the log-distance path loss model with log-normal shadowing to calculate the strength and signal-to-noise (SNR) ratio of the reflected signals. In the absence of the LoS path, the path loss between the *k*-th SP and the *m*-th sample point can be written as

$$PL^m_k\,(dB) = \beta_0 + 10\alpha_N \log(l^m_k) + \psi_N, \tag{3}$$

where $\beta_0 = 20\log\left(\frac{4\pi f_c}{c}\right)$ is the reference path loss at a distance of 1m; f_c and c are the main frequency of the A2G channel and the speed of light, respectively; α_N is the path loss exponent (PLE) when the LoS path does not exist; $l^m_k = \sqrt{(h_B - h^m_U)^2 + \|\mathbf{w}_k - \mathbf{u}_m\|^2}$ is the 3-D distance between the SP and the sample point; $\psi_N \sim \mathcal{N}\left(0, \sigma_N^2\right)$ is a Gaussian random variable representing the log-normal shadowing, and σ_N^2 is its variance. In practice, the values of parameters α_N and σ_N^2 can be set or changed flexibly according to the local environment. As will be described in Appendix A, the proposed system uses TWR-based positioning to locate the ground user. The implementation of TWR requires the exchange of messages between two devices [52], which means that both the UAV platform and the user need to transmit and receive the PRS signal. In practical applications, the transceiver carried by the UAV platform tends to have a larger transmit power than user's handheld device, which means that the signal transmitted by the latter is more difficult to detect. Therefore, the occurrence of NLoS condition depends directly on the SNR of the reflected signals transmitted by the user device and received at the UAV platform, which can be expressed as

$$SNR^m_{k,U\to B}\,(dB) = P_{t,U} - PL^m_k - P_{n_0}, \tag{4}$$

where $P_{t,U}$ denotes the constant transmit power of user device in dBm, and P_{n_0} is the noise power in dBm. The reflected signals are considered to be detectable if the corresponding SNR exceeds a threshold $SNR_{\min}$, whose value is related to the sensitivity of the airborne transceiver. It is worth noting that although the distance between the SP and the sample point is known, the detection of reflected signals is still a random event due to the shadowing component ψ_N in (3). In addition, we assume that the terrain uncertainty and the shadowing are independent of each other. Thus, the prior probability of the NLoS condition is defined as the joint probability that the LoS path does not exist and $SNR^m_{k,U\to B}$ exceeds $SNR_{\min}$, which can be expressed as

$$\begin{aligned} P^m_{k,NLoS} &= P\left(SNR^m_{k,U\to B} > SNR_{\min}, No\_LoS\right) \\ &= P^m_{k,No\_LoS}\cdot P\left(SNR^m_{k,U\to B} > SNR_{\min} \middle| No\_LoS\right) \\ &= P^m_{k,No\_LoS}\cdot P(\psi_N < \psi_{\max}) \\ &= P^m_{k,No\_LoS}\cdot F_{\psi_N}(\psi_{\max}), \end{aligned} \tag{5}$$

where

$$\psi_{\max} = (P_{t,U} - P_{n_0} - SNR_{\min}) - (\beta_0 + 10\alpha_N \log(l^m_k)). \tag{6}$$

Moreover, the prior probability of blockage condition is given by

$$\begin{aligned} P^m_{k,B} &= P\left(SNR^m_{k,U\to B} \le SNR_{\min}, No\_LoS\right) \\ &= P^m_{k,No\_LoS}\cdot\left(1 - F_{\psi_N}(\psi_{\max})\right) \\ &= 1 - P^m_{k,LoS} - P^m_{k,NLoS}. \end{aligned} \tag{7}$$

As long as the DEM of the local environment is available, the prior probability of each propagation condition corresponding to the A2G channel between the *k*-th SP and *m*-th sample point can be obtained utilizing equations (2), (5) and (7).

B. Model of Service Failure

In the proposed system, the potential conditions in the range measurement between the *k*-th SP and *m*-th sample point can be divided into three categories: 1) blockage condition (B), 2) failure condition (F) and 3) normal condition (N). As analyzed in subsection A, the prior probability of blockage condition is

[1]Before calculating $\Delta h^m_{k,\min}$, those DEM data points within 20 meters of the ground user are excluded in advance. The reason for doing this is to avoid the unrealistic situation where the propagation condition is only determined by the DEM data point closest to the user.

$P^m_{k,B}$. Thus, the prior probability that the range measurement can be obtained (O) is $P^m_{k,O} = 1 - P^m_{k,B}$. In this article, the NLoS propagation and internal faults are considered as the two major causes of service failures, and are independent of each other. The prior probability of internal fault P_{IF} could be determined in advance based on the reliability of the airborne transceiver and user device, and will not change during the positioning process. Thus, the prior probability of failure condition is given by

$$P^m_{k,F} = P^m_{k,LoS} P_{IF} + P^m_{k,NLoS}. \tag{8}$$

The prior probability of normal condition where neither NLoS propagation nor internal fault occurs can be expressed as

$$P^m_{k,N} = P^m_{k,Los} \cdot (1 - P_{IF}). \tag{9}$$

Moreover, the conditional probabilities of failure and normal conditions in the presence of range measurement are denoted as $P^m_{k,F|O} = P^m_{k,F} \big/ P^m_{k,O}$ and $P^m_{k,N|O} = P^m_{k,N} \big/ P^m_{k,O}$, respectively.

The proposed system utilizes TWR-based method to provide positioning services, whose measurement model will be introduced in detail in Appendix A. The influence of NLoS propagation and internal faults on TWR can be modeled as significant biases introduced in range measurements. Thus, the expression of range measurement under failure conditions can be written as

$$\hat{l}_k = \sqrt{(h_B - h_U)^2 + \|\mathbf{w}_k - \mathbf{u}\|^2} + n_C + b_k, \quad k \in \mathcal{K}. \tag{10}$$

It is worth noting that if the measurement bias b_k is only caused by NLoS propagation, its value is always positive. Otherwise, the value of b_k could be either positive or negative. In practice, the absolute value of the bias b_k is typically much larger than that of the measurement noise n_C. Although it is possible that the positive bias of NLoS propagation and the negative bias caused by internal faults cancel each other out exactly, the probability of such events is extremely small and will not be considered in the following.

III. Reliability Prediction for UAV-Enabled Positioning

There are many mature techniques that can be used in the proposed system to detect online failures [32], [33]. Besides, during the positioning process, the reliability (i.e., the minimum detectable error) of failure detection can be evaluated in real time utilizing the methods presented in existing research [34]. Thus, the focus of this section is not online fault detection or reliability evaluation, but the offline reliability prediction before the UAV takes off. For the proposed system, if the UAV is launched without adequate reliability prediction, the reliability of failure detection and the accuracy of positioning results are very likely to fail to meet the mission requirements, resulting in a waste of time and resources (fuel or battery). Therefore, it is necessary to perform reliability prediction before the mission starts. However, compared with the online reliability evaluation, the realization of the offline reliability prediction is much more difficult. The major challenge is that due to the uncertainty of user's location and probabilistic propagation condition, it is impossible to determine whether the range measurement corresponding to a certain SP could be obtained or not (i.e., the observation condition) before the TWR is performed.

This section presents our proposed reliability prediction method. The failure detection method used in this article is introduced in subsection A. Then, in subsection B, we divide all possible events in the positioning process into multiple "observation events" and "failure events" according to the visibility and status (normal or failure) of each SP, and the prior probability of each event is derived. Finally, the reliability of the positioning service is predicted based on the minimum detectable error in each failure event.

In addition, we assume that the mission requires the proposed system to detect failures that cause a position error larger than η_{REQ} in either x- or y-direction. The tolerable false alarm (FA) rate and missed detection (MD) rate are denoted by P^{REQ}_{FA} and P^{REQ}_{MD}, respectively.

A. Failure Detection based on LS-Residuals

In this article, the least-squares-residuals (LS) method, a well-known fault detection method originally developed for GNSS applications [32], [34], is applied to the proposed system to detect failures. We assume that during the mission, the UAV platform can obtain range measurements at N SPs. Then, the basic measurement equation used in the LS method is obtained through the linearization of equation (10), which can be expressed as

$$\mathbf{l}_* = \mathbf{H}_* \mathbf{u} + \mathbf{n}_* + \mathbf{b}_*, \tag{11}$$

where $\mathbf{l}_* = \left[\hat{l}_1, \cdots, \hat{l}_N\right]^T$ is the $N \times 1$ measurement vector, and $\hat{l}_k$ represents the range measurement corresponding to the k-th SP; $\mathbf{u} = [x_U, y_U]^T$ is the 2×1 state vector, representing the unknown horizontal coordinate of the ground user; $\mathbf{H}_* = \left[\left(\partial \hat{l}_1 \big/ \partial \mathbf{u}\right)^T, \cdots, \left(\partial \hat{l}_N \big/ \partial \mathbf{u}\right)^T\right]^T$ is the $N \times 2$ Jacobian matrix of ranging equations; $\mathbf{n}_*$ is the $N \times 1$ vector of zero-mean Gaussian measurement noise due to the clock drift, and its covariance matrix is denoted by $\mathbf{V}_* = \sigma_C^2 \cdot \mathbf{I}_N$; $\mathbf{b}_*$ is the $N \times 1$ fault vector composed of measurement biases caused by faults, and $\mathbf{b}_* = \mathbf{0}_{N \times 1}$ under normal conditions. For the sake of convenience, we normalize the above equation with the covariance matrix $\mathbf{V}_*$ [34]. The normalized measurement equation is given by

$$\mathbf{l} = \mathbf{H}\mathbf{u} + \mathbf{n} + \mathbf{b}, \tag{12}$$

where $\mathbf{I} = \mathbf{V}_*^{-1/2} \mathbf{I}_*$, $\mathbf{H} = \mathbf{V}_*^{-1/2} \mathbf{H}_*$, $\mathbf{n} = \mathbf{V}_*^{-1/2} \mathbf{n}_*$ and $\mathbf{b} = \mathbf{V}_*^{-1/2} \mathbf{b}_*$. After normalization, the covariance matrix ($\mathbf{V}$) of the noise vector $\mathbf{n}$ becomes an $N \times N$ identity matrix, that is, $\mathbf{n} \sim \mathcal{N}(\mathbf{0}_{N \times 1}, \mathbf{I}_N)$. Then, the least-squares solution of the normalized equation can be expressed as

$$\hat{\mathbf{u}} = \left(\mathbf{H}^T \mathbf{H}\right)^{-1} \mathbf{H}^T \mathbf{l} = \mathbf{G}\mathbf{l}. \tag{13}$$

Specifically, the estimated x- and y-coordinates can be written as [34]

$$\hat{x}_U = \boldsymbol{\alpha}_x^T \hat{\mathbf{u}} = \mathbf{s}_x^T \mathbf{l}, \tag{14}$$

$$\hat{y}_U = \boldsymbol{\alpha}_y^T \hat{\mathbf{u}} = \mathbf{s}_y^T \mathbf{l}, \tag{15}$$

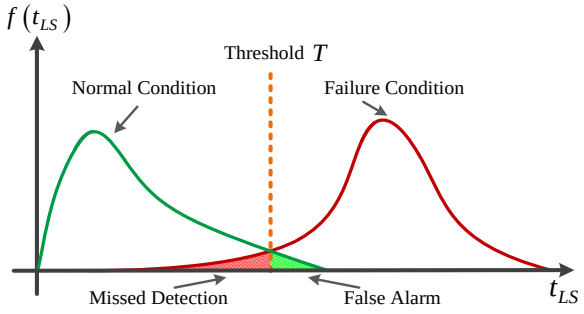

Fig. 8. Distributions of the test statistic.

where $\boldsymbol{\alpha}_x = [1,0]^T$, $\boldsymbol{\alpha}_y = [0,1]^T$, $\mathbf{s}_x^T = \boldsymbol{\alpha}_x^T \mathbf{G}$ and $\mathbf{s}_y^T = \boldsymbol{\alpha}_y^T \mathbf{G}$.

The expression and distribution of the estimate error are given by

$$\boldsymbol{\varepsilon} = \hat{\mathbf{u}} - \mathbf{u} = \mathbf{G}(\mathbf{H}\mathbf{u} + \mathbf{n} + \mathbf{b}) - \mathbf{u} = \mathbf{G}(\mathbf{n} + \mathbf{b}), \tag{16}$$

$$\varepsilon_x = \boldsymbol{\alpha}_x^T \boldsymbol{\varepsilon} = \mathbf{s}_x^T(\mathbf{n} + \mathbf{b}), \quad \varepsilon_y = \boldsymbol{\alpha}_y^T \boldsymbol{\varepsilon} = \mathbf{s}_y^T(\mathbf{n} + \mathbf{b}), \tag{17}$$

$$\varepsilon_x \sim \begin{cases} \mathcal{N}(0, \mathbf{s}_x^T \mathbf{s}_x), & \text{Normal condition,} \\ \mathcal{N}(\mathbf{s}_x^T \mathbf{b}, \mathbf{s}_x^T \mathbf{s}_x), & \text{Failure condition.} \end{cases} \tag{18}$$

It can be clearly seen from the above equations that faults do introduce a large bias in the positioning result, meaning that the location estimator is no longer unbiased. To address this problem, the LS method performs the failure detection based on the differences (residuals) between the actual measured ranges and the predicted ranges, which can be expressed as

$$\hat{\mathbf{l}} = \mathbf{H}\hat{\mathbf{u}} = \mathbf{H}\mathbf{G}\mathbf{l}, \tag{19}$$

$$\mathbf{r} = \mathbf{l} - \hat{\mathbf{l}} = (\mathbf{I}_N - \mathbf{H}\mathbf{G})\mathbf{l} = (\mathbf{I}_N - \mathbf{H}\mathbf{G})(\mathbf{n} + \mathbf{b}), \tag{20}$$

where $\hat{\mathbf{l}}$ is the $N \times 1$ vector of predicted ranges based on the estimated location, and $\mathbf{r}$ is the residual vector. The squared norm of the vector $\mathbf{r}$ is employed as the test statistic for failure detection, which can be written as

$$t_{LS} \triangleq \|\mathbf{r}\|^2 = \mathbf{r}^T \mathbf{r}. \tag{21}$$

Under normal conditions, the test statistic t_{LS} is the sum of the squares of multiple Gaussian random variables, which are obtained through a linear transformation of another set of independent zero-mean Gaussian variables with the same variance. Thus, t_{LS} follows a chi-square distribution (green solid line in Fig. 8) with $N-2$ degrees of freedom (DOF). Under failure conditions, t_{LS} has a non-central chi-square distribution (red solid line). The distributions of test statistic t_{LS} under normal and failure conditions can be expressed as follows:

$$t_{LS} \sim \begin{cases} \chi^2(N-2), & \text{Normal condition,} \\ \chi^2(N-2, \mathbf{b}^T(\mathbf{I} - \mathbf{H}\mathbf{G})\mathbf{b}), & \text{Failure condition.} \end{cases} \tag{22}$$

As shown in Fig. 8, if we set a decision threshold T for the test statistic t_{LS}, the failure detection can be realized with the following decision rule:

If: $t_{LS} \geq T$, declare "service failure.";
If: $t_{LS} < T$, declare "service succeed.".

B. Observation Events and Failure Events

Before the mission starts, the visibility of SPs is unknown. In other words, we cannot be sure whether the UAV platform can obtain the desired range measurement at a certain SP. However, there is no doubt that the number and geometry of available SPs will affect the reliability of failure detection. Therefore, every possible observation event must be taken into consideration when making reliability prediction, as shown in Fig. 9.

Assume that the system has set K SPs for the UAV, then the number of possible observation events is $G = 2^K$. Among all observation events, there are $G_{SU} = \binom{K}{2} + \binom{K}{1} + 1$ "service-unavailable (SU)" events in which the available SPs are too few to support the positioning service. Moreover, in $G_{PO} = \binom{K}{3}$ "positioning-only (PO)" observation events, the number of available SPs is just enough for the positioning service but still not enough for failure detection. Excluding the above two types of events, the remaining $G_R = G - G_{SU} - G_{PO}$ observation events in which the failure detection function can be implemented are represented by the set

$$\mathcal{O} = \{\mathbf{o}_1, \mathbf{o}_2, \cdots, \mathbf{o}_{G_R}\}, \tag{23}$$

where the subset

$$\mathbf{o}_g = \left\{a_1^g, \cdots, a_{A_g}^g, u_1^g, \cdots, u_{U_g}^g\right\} \tag{24}$$

denotes the g-th observation event with A_g available SPs and U_g unavailable SPs ($A_g + U_g = K$); a_i^g and u_j^g are the index numbers of the i-th available SP and j-th unavailable SP in observation event $\mathbf{o}_g$, respectively. For the m-th sample point of the user's location, the prior probability of the g-th observation event is given by

$$P_g^m = \prod_{i=1}^{A_g} P_{a_i^g, O}^m \cdot \prod_{j=1}^{U_g} P_{u_j^g, B}^m, \tag{25}$$

where the expressions of $P_{a_i^g, O}^m$ and $P_{u_j^g, B}^m$ are derived in Section II. Moreover, the conditional FA rate corresponding to the g-th observation event can be expressed as

$$\begin{aligned} P_{FA|\mathbf{o}_g}^m &= P(|\varepsilon_x| < \eta \cap |\varepsilon_y| < \eta \cap t_{LS} \geq T_g | \mathbf{o}_g, \mathbf{b} = \mathbf{0}) \\ &< P(t_{LS} \geq T_g | \mathbf{o}_g, \mathbf{b} = \mathbf{0}_{A_g \times 1}) \\ &= \int_{T_g}^{+\infty} \chi_t^2(A_g - 2, 0) dt, \end{aligned} \tag{26}$$

where T_g is the decision threshold for failure detection in observation event $\mathbf{o}_g$.

As analyzed in Section II.B, each range measurement obtained in the positioning process may be contaminated by failure. As shown in Fig. 9, according to the status of each SP, the observation event $\mathbf{o}_g$ can be further subdivided into one normal event in which no failure occurs and $Q_g = 2^{A_g} - 1$ failure events. The prior probability of the normal event $\mathbf{f}_0^g$ is given by

$$P_{g,0}^m = P_g^m \cdot P_{0|g}^m = P_g^m \cdot \prod_{i=1}^{A_g} P_{a_i^g, N|O}^m. \tag{27}$$

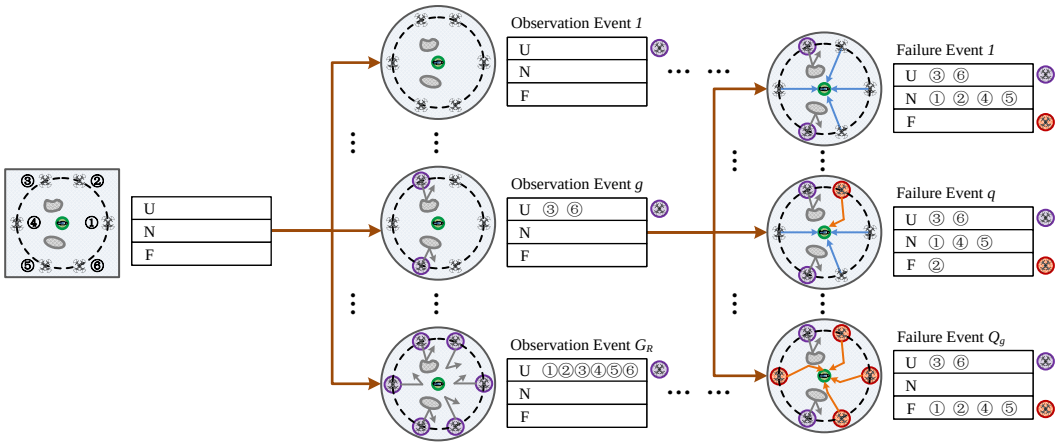

Fig. 9. Event tree: "U" indicates that the measurement is unavailable; "N" and "F" represent the normal and failure conditions, respectively.

All potential failure events in the g-th observation event can be represented by the set

$$\mathcal{F}_g = \left\{ \mathbf{f}_1^g, \mathbf{f}_2^g, \cdots, \mathbf{f}_{Q_g}^g \right\}, \tag{28}$$

where the subset

$$\mathbf{f}_q^g = \left\{ n_1^{g,q}, \cdots, n_{N_q^g}^{g,q}, f_1^{g,q}, \cdots, f_{F_q^g}^{g,q} \right\} \tag{29}$$

denotes the q-th failure event in observation event $\mathbf{o}_g$, in which there are N_q^g normal SPs and F_q^g failure SPs ($N_q^g + F_q^g = A_g$); $n_i^{g,q}$ and $f_j^{g,q}$ are the index numbers of the i-th normal SP and j-th failure SP in failure event $\mathbf{f}_q^g$, respectively. For the m-th sample point, the prior probability of the q-th failure event is given by

$$P_{g,q}^m = P_g^m \cdot P_{q|g}^m = P_g^m \cdot \prod_{i=1}^{N_q^g} P_{n_i^{g,q},N|O}^m \cdot \prod_{j=1}^{F_q^g} P_{f_j^{g,q},F|O}^m, \tag{30}$$

where the expressions of conditional probabilities $P_{n_i^{g,q},N|O}^m$ and $P_{f_j^{g,q},F|O}^m$ can be found in Section II.B. It is noteworthy that for any failure event, there is a certain probability that the failure is not successfully detected, that is, the MD rate. The conditional MD rate corresponding to failure event $\mathbf{f}_q^g$ can be expressed as

$$\begin{aligned} P_{MD|\mathbf{f}_q^g}^m &= P\left((|\varepsilon_x| \geq \eta \cup |\varepsilon_y| \geq \eta) \cap (t_{LS} < T_g) | \, \mathbf{f}_q^g \right) \\ &< P\left(|\varepsilon_x| \geq \eta \cap t_{LS} < T_g | \, \mathbf{f}_q^g \right) \\ &\quad + P\left(|\varepsilon_y| \geq \eta \cap t_{LS} < T_g | \, \mathbf{f}_q^g \right). \end{aligned} \tag{31}$$

C. Reliability Prediction and the Corresponding Metric

The proposed reliability prediction method is summarized in *Algorithm 1* shown in Appendix B. It can be seen that the implementation of this method can be divided into four stages: "initialization", "event classification", "requirement allocation" and "reliability prediction". The operations in the first two stages have been introduced above. In this subsection, we mainly describe the technical details of the remaining two stages.

As mentioned in the previous subsection, for the proposed system, all possible events in the positioning process can be divided into several observation events, each of which can be further subdivided into multiple failure events. However, the mission requirement only gives the tolerable limits of overall FA and MD rates, and does not specify the tolerable conditional FA/MD rate corresponding to each observation event/failure event. As can be seen from equation (26), the conditional FA rate of each observation event $\mathbf{o}_g$ mainly depends on the value of the decision threshold T_g. From another perspective, if the tolerable conditional FA rate $P_{FA|\mathbf{o}_g}^{REQ}$ is given, the feasible region of decision threshold can be determined according to the constraint $P_{FA|\mathbf{o}_g}^m \leq P_{FA|\mathbf{o}_g}^{REQ}$. In practical applications, the decision threshold is typically set to the value that just satisfies the constraint, that is,

$$\int_{T_g}^{+\infty} \chi_t^2 \left(A_g - 2, 0 \right) dt = P_{FA|\mathbf{o}_g}^{REQ}. \tag{32}$$

It can be clearly seen from the above equation that the allocation of tolerable FA rate among observation events determines the values of decision thresholds, thereby affecting the results of reliability prediction. Thus, in this section, we first introduce the FA rate allocation scheme (*Algorithm 2* in Appendix B) adopted in the proposed reliability prediction method.

In the reliability prediction process, the overall FA rate is defined as the sum of the conditional FA rates of all possible observation events weighted by the prior probabilities of corresponding normal events, that is,

$$P_{FA}^m \triangleq \sum_{g=1}^{G_R} P_{FA|\mathbf{o}_g}^m \cdot P_{g,0}^m + P_{FA,PO}^m, \tag{33}$$

where $P_{FA,PO}^m$ is the FA rate of G_{PO} "positioning-only" observation events. Once these events occur, the system will sound an alarm. Thus, the MD rate of these observation events is 0, and their FA rate can be approximated by their prior probability. In addition, for those service unavailable observation events, their FA and MD rates are both 0. Then, according to the mission requirement ($P_{FA}^m \leq P_{FA}^{REQ}$) mentioned at the

beginning of this section, the allocation of tolerable FA rate should satisfy the following constraint:

$$\sum_{g=1}^{G_R} P_{FA|\mathbf{o}_g}^{REQ} \cdot P_{g,0}^m \leq P_{FA}^{REQ} - P_{FA,PO}^m. \tag{34}$$

When allocating the tolerable FA rate, we first sort the observation events in ascending order of the prior probabilities of corresponding normal events. The sorted observation events and corresponding prior probabilities are, respectively, denoted by the sets

$$\bar{\mathcal{O}} = \{\bar{\mathbf{o}}_1, \bar{\mathbf{o}}_2, \cdots, \bar{\mathbf{o}}_{G_R}\}, \tag{35}$$

$$\bar{\mathcal{P}}_0^m = \left\{\bar{P}_{1,0}^m, \bar{P}_{2,0}^m, \ldots, \bar{P}_{G_R,0}^m\right\}, \tag{36}$$

and $\bar{P}_{g-1,0}^m \leq \bar{P}_{g,0}^m \leq \bar{P}_{g+1,0}^m$. It is worth noting that since the SPs are carefully selected, most of the observation events in set $\bar{\mathcal{O}}$ are very unlikely to occur, that is to say, the FA rates of these events are small and negligible. The index of the first observation event that needs to be considered in the FA rate allocation can be expressed as

$$g^* = \min\left[g | \sum_{i=1}^{g} \bar{P}_{i,0}^m \geq P_{FA}^{REQ} - P_{FA,PO}^m\right]. \tag{37}$$

Then, the first $g^* - 1$ observation events in set $\bar{\mathcal{O}}$ are excluded. Specifically, the tolerable conditional FA rates $P_{FA|\mathbf{o}_g}^{REQ}$ $(1 \leq g < g^*)$ of these observation events are set to 1, whereas their conditional MD rates are 0. After excluding these observation events, the constraint on FA rate allocation among the remaining events can be written as

$$\sum_{g=g^*}^{G_R} P_{FA|\bar{\mathbf{o}}_g}^{REQ} \cdot \bar{P}_{g,0}^m \leq P_{FA}^{REQ} - P_{FA,PO}^m - P_{FA,EXL}^{REQ}, \tag{38}$$

where $P_{FA,EXL}^{REQ} = \sum_{g=1}^{g^*-1} 1 \cdot \bar{P}_{g,0}^m$ denotes the tolerable FA rate of those excluded observation events. Finally, the remaining tolerable FA rate $(P_{FA}^{REQ} - P_{FA,PO}^m - P_{FA,EXL}^{REQ})$ is allocated according to the prior probabilities of the remaining normal events, and the FA rate allocated to event $\bar{\mathbf{o}}_g$ $(g^* \leq g \leq G_R)$ is given by

$$\begin{aligned} P_{FA,\bar{\mathbf{o}}_g}^{REQ} &= P_{FA|\bar{\mathbf{o}}_g}^{REQ} \cdot \bar{P}_{g,0}^m \\ &= \frac{\left(P_{FA}^{REQ} - P_{FA,PO}^m - P_{FA,EXL}^{REQ}\right) \cdot \bar{P}_{g,0}^m}{\sum_{i=g^*}^{G_R} \bar{P}_{i,0}^m}. \end{aligned} \tag{39}$$

After the tolerable conditional FA rate of each observation event $(P_{FA|\bar{\mathbf{o}}_g}^{REQ} = P_{FA,\bar{\mathbf{o}}_g}^{REQ} \Big/ \bar{P}_{g,0}^m)$ is determined, the corresponding decision threshold T_g can be obtained utilizing equation (32).

It can be seen from equation (31) that once the decision threshold is determined, the conditional MD rate of each failure event $\mathbf{f}_q^g$ depends on the tolerable limit η of position error. From another point of view, for a certain tolerable conditional MD rate $P_{MD|\mathbf{f}_q^g}^{REQ}$, there exists a set of values of parameter η that satisfy the constraint $P_{MD|\mathbf{f}_q^g}^m \leq P_{MD|\mathbf{f}_q^g}^{REQ}$, which is called "detectable position error". The minimum detectable error (η^*) can effectively reflect the reliability of failure detection, making it extremely important in reliability prediction. In the following paragraphs, we introduce the MD rate allocation scheme (*Algorithm 3* in Appendix B) adopted in the proposed reliability prediction method.

According to the mission requirement $(P_{MD}^m \leq P_{MD}^{REQ})$, the allocation of tolerable MD rate should satisfy the following constraint:

$$\sum_{g=1}^{G_R} P_{MD,\bar{\mathbf{o}}_g}^{REQ} = \sum_{g=1}^{G_R} \sum_{q=1}^{\bar{Q}_g} P_{MD|\mathbf{f}_q^g}^{REQ} \cdot P_{g,q}^m \leq P_{MD}^{REQ}, \tag{40}$$

where the term $\sum_{g=1}^{G_R} P_{MD,\bar{\mathbf{o}}_g}^{REQ}$ means the allocation of tolerable MD rate among observation events, and the term $\sum_{q=1}^{\bar{Q}_g} P_{MD|\mathbf{f}_q^g}^{REQ} \cdot P_{g,q}^m$ represents the allocation among multiple failure events in the same observation event. We first analyze the former. As mentioned above, only the last $G_R - g^* + 1$ observation events in set $\bar{\mathcal{O}}$ need to be considered, while the tolerable conditional MD rates of the other $g^* - 1$ events are set to 0. The MD rate allocated to event $\bar{\mathbf{o}}_g$ $(g^* \leq g \leq G_R)$ is

$$P_{MD,\bar{\mathbf{o}}_g}^{REQ} = \left(P_{MD}^{REQ} \cdot \bar{P}_{g,\mathbf{f}}^m\right) \Big/ \sum_{i=g^*}^{G_R} \bar{P}_{i,\mathbf{f}}^m, \tag{41}$$

where

$$\bar{P}_{g,\mathbf{f}}^m = \sum_{q=1}^{\bar{Q}_g} \bar{P}_{g,q}^m = \bar{P}_g^m - \bar{P}_{g,0}^m \tag{42}$$

is the sum of the prior probabilities of all possible failure events in observation event $\bar{\mathbf{o}}_g$; $\bar{P}_g^m$ and $\bar{P}_{g,q}^m$ denote the prior probabilities of observation event $\bar{\mathbf{o}}_g$ and the q-th failure event in it, respectively.

Then, we further consider the MD rate allocation among multiple failure events in the same observation event $\bar{\mathbf{o}}_g$. Similar to the operation in FA rate allocation, we first sort the $\bar{Q}_g$ failure events according to their prior probabilities, and then exclude those events with negligible prior probabilities. Let $\bar{\mathcal{F}}_g = \left\{\bar{\mathbf{f}}_1^g, \bar{\mathbf{f}}_2^g, \cdots, \bar{\mathbf{f}}_{\bar{Q}_g}^g\right\}$ be the set of sorted failure events, and q^* be the index of the first failure event that needs to be considered. The constraint on MD rate allocation among the remaining $\bar{Q}_g - q^* + 1$ events can be written as

$$\sum_{q=q^*}^{\bar{Q}_g} P_{MD|\bar{\mathbf{f}}_q^g}^{REQ} \cdot \bar{P}_{g,q}^m \leq P_{MD,\bar{\mathbf{o}}_g}^{REQ} - P_{MD,EXL,\bar{\mathbf{o}}_g}^{REQ}, \tag{43}$$

where $P_{MD,EXL,\bar{\mathbf{o}}_g}^{REQ} = \sum_{q=1}^{q^*-1} 1 \cdot \bar{P}_{g,q}^m$ denotes the tolerable MD rate of those excluded failure events. Finally, the remaining tolerable MD rate $(P_{MD,\bar{\mathbf{o}}_g}^{REQ} - P_{MD,EXL,\bar{\mathbf{o}}_g}^{REQ})$ is allocated to each failure event $\bar{\mathbf{f}}_q^g$ $(q^* \leq q \leq \bar{Q}_g)$ according to its prior probability:

$$\begin{aligned} P_{MD,\bar{\mathbf{f}}_q^g}^{REQ} &= P_{MD|\bar{\mathbf{f}}_q^g}^{REQ} \cdot \bar{P}_{g,q}^m \\ &= \frac{\left(P_{MD,\bar{\mathbf{o}}_g}^{REQ} - P_{MD,EXL,\bar{\mathbf{o}}_g}^{REQ}\right) \cdot \bar{P}_{g,q}^m}{\sum_{j=q^*}^{\bar{Q}_g} \bar{P}_{g,j}^m}. \end{aligned} \tag{44}$$

In addition, in equation (31), the conditional MD rate $P^{m}_{MD|\mathbf{f}^{g}_{q}}$ is upper-bounded by the sum of the conditional MD rates in x- and y-directions. In the rest of this subsection, we will analyze the reliability of failure detection in x- and y-directions separately, and determine the minimum detectable error in each direction. Thus, the tolerable conditional MD rate ($P^{REQ}_{MD|\bar{\mathbf{f}}^{g}_{q}}$) of failure event $\bar{\mathbf{f}}^{g}_{q}$ is further equally allocated to the two directions, that is,

$$P^{REQ,x}_{MD|\bar{\mathbf{f}}^{g}_{q}} = P^{REQ,y}_{MD|\bar{\mathbf{f}}^{g}_{q}} = P^{REQ}_{MD|\bar{\mathbf{f}}^{g}_{q}} \Big/ 2, \tag{45}$$

where $P^{REQ,x}_{MD|\bar{\mathbf{f}}^{g}_{q}}$ and $P^{REQ,y}_{MD|\bar{\mathbf{f}}^{g}_{q}}$ denote the conditional MD rates allocated to the x- and y-directions, respectively.

In the proposed system, the minimum detectable position error in all possible failure events and both directions is taken as the metric for reliability prediction. We first take the failure detection in x-direction as an example to analyze the minimum detectable error in failure event $\bar{\mathbf{f}}^{g}_{q}$. The key to determining the minimum detectable error is to find the worst fault vector that maximizes the position error while satisfying the constraint of tolerable conditional MD rate, that is,

$$\begin{aligned} \max_{\mathbf{b}^{g}_{q}} \quad & |\varepsilon_x| \\ \text{s.t.} \quad & P\left(t_{LS} < T_g | \, \mathbf{b}^{m,x}_{g,q}\right) \le P^{REQ,x}_{MD|\bar{\mathbf{f}}^{g}_{q}}, \end{aligned} \tag{46}$$

where $\mathbf{b}^{m,x}_{g,q}$ denotes the fault vector in failure event $\bar{\mathbf{f}}^{g}_{q}$. Noted that in the above equation, the conditional MD rate $P\left(|\varepsilon_x| \ge \eta \cap t_{LS} < T_g | \, \mathbf{b}^{m,x}_{g,q}\right)$ is replaced by the term $P\left(t_{LS} < T_g | \, \mathbf{b}^{m,x}_{g,q}\right)$ since $P\left(|\varepsilon_x| \ge \eta \cap t_{LS} < T_g | \, \mathbf{b}^{m,x}_{g,q}\right) \le P\left(t_{LS} < T_g | \, \mathbf{b}^{m,x}_{g,q}\right)$. As mentioned in [53], the worst fault vector is also the one with the largest "failure slope (s)". The slope s is defined as the ratio of the squared mean of the position error ε_x over the non-centrality parameter of the test statistic t_{LS}, and can be written as

$$s \triangleq \frac{\mathbf{b}^T \mathbf{s}_x \mathbf{s}_x^T \mathbf{b}}{\mathbf{b}^T \left(\mathbf{I} - \mathbf{H}\mathbf{G}\right) \mathbf{b}}. \tag{47}$$

The methods for calculating the worst fault vector and the corresponding slope were described in [34] and will not be repeated here. Let $\mathbf{b}^{*m,x}_{g,q}$ be the worst fault vector, and $s^{*m,x}_{g,q}$ be the largest failure slope. Then, the minimum detectable error in the x-direction in event $\bar{\mathbf{f}}^{g}_{q}$ is defined as the estimate bias cause by the worst fault vector, and can be expressed as

$$\eta^{*m,x}_{g,q} \triangleq \sqrt{s^{*m,x}_{g,q} \cdot \left(\mathbf{b}^{*m,x}_{g,q}\right)^T \left(\mathbf{I} - \mathbf{H}_g \mathbf{G}_g\right) \left(\mathbf{b}^{*m,x}_{g,q}\right)}, \tag{48}$$

where $\mathbf{H}_g$ is the Jacobian matrix of the normalized ranging equations in observation event $\bar{\mathbf{o}}_g$, and $\mathbf{G}_g = \left(\mathbf{H}_g^T \mathbf{H}_g\right)^{-1} \mathbf{H}_g^T$. With the above operations, we can also determine the minimum detectable error $\eta^{*m,y}_{g,q}$ in the y-direction.

For the m-th sample point of user's location, its corresponding reliability prediction result is defined as the largest of the minimum detectable errors in all possible failure events, which can be expressed as

$$\eta^{*m} = \max_{g \in \mathcal{G}} \left\{ \max_{q \in \bar{\mathcal{Q}}_g} \left\{ \eta^{*m,x}_{g,q}, \eta^{*m,y}_{g,q} \right\} \right\}, \tag{49}$$

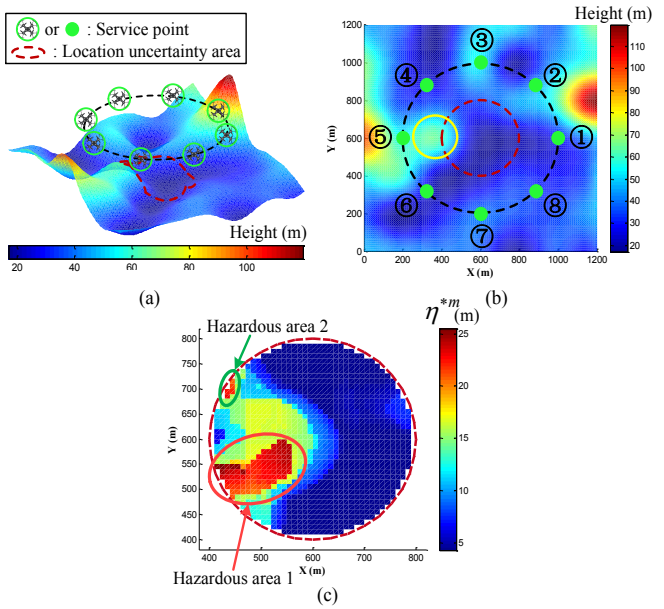

Fig. 10. Example of reliability prediction: (a) 3-D view and (b) top view of the test scenario, and (c) the corresponding prediction results (η^{*m}).

where $\mathcal{G} = \{g^*, \cdots, G_R\}$, and $\bar{\mathcal{Q}}_g = \{q^*, \cdots, \bar{Q}_g\}$. The prediction results in x- and y-directions can be written as

$$\eta^{*m,x} = \max_{g \in \mathcal{G}} \left\{ \max_{q \in \bar{\mathcal{Q}}_g} \left\{ \eta^{*m,x}_{g,q} \right\} \right\}, \tag{50}$$

$$\eta^{*m,y} = \max_{g \in \mathcal{G}} \left\{ \max_{q \in \bar{\mathcal{Q}}_g} \left\{ \eta^{*m,y}_{g,q} \right\} \right\}. \tag{51}$$

Moreover, as mentioned at the beginning of Section II, the uncertainty area of the user's location contains M sample points, and the prior probability of the user being located at each sample point is equal. Thus, the worst predicted reliability in all sample points is taken as the prediction result of service reliability, that is

$$\eta^{*} = \max_{m \in \mathcal{M}} \left\{ \eta^{*m} \right\} = \max_{m \in \mathcal{M}} \left\{ \eta^{*m,x}, \eta^{*m,y} \right\}. \tag{52}$$

With the proposed reliability prediction method and the derived metric, system operators and mission commanders are capable of evaluating the reliability of positioning service before the mission starts, which is beneficial for decision-making. If the predicted detectable position error η^{*} does not exceed the mission's tolerable limit η_{REQ}, the UAV is permitted to take off and provide service. This is because those failures that cause unacceptable position errors will be successfully detected in the positioning process and will not mislead decision-makers.

IV. Preliminary Study on Reliability Enhancement

In mountainous environments with complex and highly variable terrain, the mission's requirements for service reliability are often difficult to meet, even for a set of carefully selected SPs. Fig. 10 shows the reliability prediction results obtained in a test scenario, where the tolerable limit of position

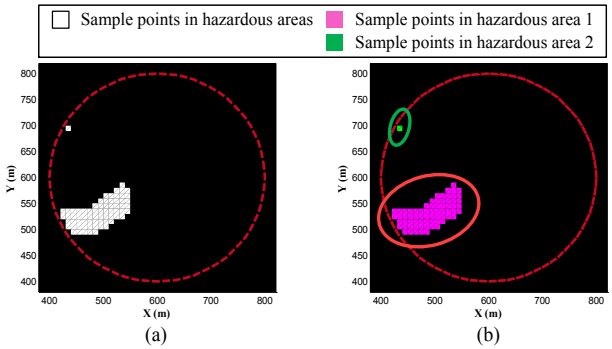

Fig. 11. Hazardous area (a) identification and (b) segmentation.

error (η_{REQ}) is set to 20m. It can be clearly seen that in the location uncertainty area, there are many sample points whose predicted detectable errors exceed η_{REQ}. If the user happens to be located at one of these sample points, failures that cause position errors larger than η_{REQ} may not be effectively detected during the positioning process, making the positioning result unreliable. Therefore, it is necessary to improve the reliability prediction results by appropriately adjusting the locations of some SPs, that is, the reliability enhancement.

The following two subsections introduce our preliminary study on reliability enhancement. In subsection A, we describe the data preprocessing procedures performed at the beginning of reliability enhancement. Subsection B presents our proposed voting-based method, which can be used to analyze the causes of unsatisfactory reliability and provide guidance for how to adjust the SPs accordingly.

A. Identification and Segmentation of Hazardous Areas

As can be seen from Fig. 10(c), sample points with unsatisfactory reliability are spatially clustered into two small blocks, which are called the "hazardous areas" in this article. The aim of reliability enhancement is to analyze the causes of these areas and eliminate them based on the analysis results. Obviously, different hazardous areas may have different causes. Therefore, the identification and segmentation of hazardous areas are two essential data preprocessing procedures for reliability enhancement.

In this article, the identification of hazardous areas is realized by comparing the reliability prediction result (η^{*m}) of each sample point m with a predetermined threshold η_T. The decision rule can be expressed as

$$m \in \begin{cases} \mathcal{M}_H, & \text{if } \eta^{*m} > \eta_T, \\ \mathcal{M}_0, & \text{otherwise}, \end{cases} \tag{53}$$

where $\mathcal{M}_H$ and $\mathcal{M}_0$ are sets composed of sample points inside and outside the hazardous areas, respectively. It is worth noting that the threshold η_T is usually set to be slightly smaller than η_{REQ}, that is, $\eta_T < \eta_{REQ}$. The reason for this is to provide a margin against the reliability degradation outside the hazardous areas caused by the adjustment of SPs' locations. Fig. 11(a) shows the result of the hazardous area identification.

After finishing the identification process, we consider how to determine which area a sample point belongs to, that is, the segmentation of the hazardous area. In this article, the well-known 8-connected neighborhood approach is used to determine the boundary of each hazardous area and segment sample points. The segmentation results are shown in Fig. 11(b).

B. Proposed Voting-based Cause Analysis Method for Reliability Enhancement

Intuitively speaking, the major cause of hazardous areas in the test scenario is that the mountain surrounded by the yellow circle in Fig. 10(b) reduces the visibility of several SPs and increases the probability of NLoS propagation. However, this kind of intuitive analysis is not sufficient to provide guidance for the adjustment of SPs' locations and is not suitable for complex terrain environments. In order to achieve the goal of eliminating hazardous areas in the reliability prediction results, it is extremely important to find out the specific cause of each hazardous area. Specifically, we need to know which SPs' low visibility or high failure rates lead to the existence of a certain hazardous area.

It is worth noting that even the cause analysis for a single hazardous area is not easy to implement. For example, hazardous area 1 in Fig. 10(c) covers a large area and contains a number of sample points. The reasons for the unsatisfactory reliability of these sample points are very unlikely to be the same. However, it is obviously impossible to adjust SPs' locations according to the requirements of each sample point. To address this problem, we propose a voting-based cause analysis method, which can fuse the causes of all sample points inside a hazardous area into a final cause analysis result corresponding to the whole area. The proposed method is summarized in *Algorithm 4* shown in Appendix C. The key idea of this method is to let each sample point vote for the SPs that have the greatest impacts on its reliability, and the SPs with weighted votes more than a threshold value (0.5) will be regarded as the cause of the hazardous area. As can be seen from *Algorithm 4*, there are four types of voting vectors in the proposed method, namely, $\mathbf{v}^{*x}_{H_i,U}$, $\mathbf{v}^{*y}_{H_i,U}$, $\mathbf{v}^{*x}_{H_i,F|O}$ and $\mathbf{v}^{*y}_{H_i,F|O}$. $\mathbf{v}^{*x}_{H_i,U}[k] = 1$ means that the low visibility of the k-th SP is one of the reasons for the i-th hazardous area's unsatisfactory reliability in x-direction. $\mathbf{v}^{*x}_{H_i,F|O}[k] = 1$ indicates that the high conditional failure rate of the k-th SP leads to the poor reliability of the i-th hazardous area in x-direction. The vectors $\mathbf{v}^{*y}_{H_i,U}$ and $\mathbf{v}^{*y}_{H_i,F|O}$ have similar meanings to $\mathbf{v}^{*x}_{H_i,U}$ and $\mathbf{v}^{*x}_{H_i,F|O}$, respectively. Table IV shows the voting results corresponding to the test scenario. Note that the voting vectors in Table IV have been converted to binary form in the last step of *Algorithm 4*. It can be concluded that the low visibility of SPs 3, 4 and 5 is the major cause of hazardous area 1. The low visibility of SPs 6, 7 and the high conditional failure rate of SP 5 lead to the poor reliability of hazardous area 2.

The cause analysis results obtained by the proposed method provide helpful guidance for the adjustment of SPs locations. For hazardous area 1, its reliability is limited by the visibility

TABLE IV
VOTING RESULTS IN THE CAUSE ANALYSIS OF HAZARDOUS AREAS

	SP1	SP2	SP3	SP4	SP5	SP6	SP7	SP8
$\mathbf{v}^{*x}_{H_1,U}$	0	0	0	1	1	0	0	0
$\mathbf{v}^{*x}_{H_1,F\|O}$	0	0	0	1	1	0	0	0
$\mathbf{v}^{*y}_{H_1,U}$	0	0	1	1	0	0	0	0
$\mathbf{v}^{*x}_{H_1,F\|O}$	0	0	1	1	1	0	0	0
$\mathbf{v}^{*x}_{H_2,U}$	0	0	0	0	0	0	0	0
$\mathbf{v}^{*x}_{H_2,F\|O}$	0	0	0	0	0	0	0	0
$\mathbf{v}^{*y}_{H_2,U}$	0	0	0	0	0	1	1	0
$\mathbf{v}^{*x}_{H_2,F\|O}$	0	0	0	0	1	1	0	0

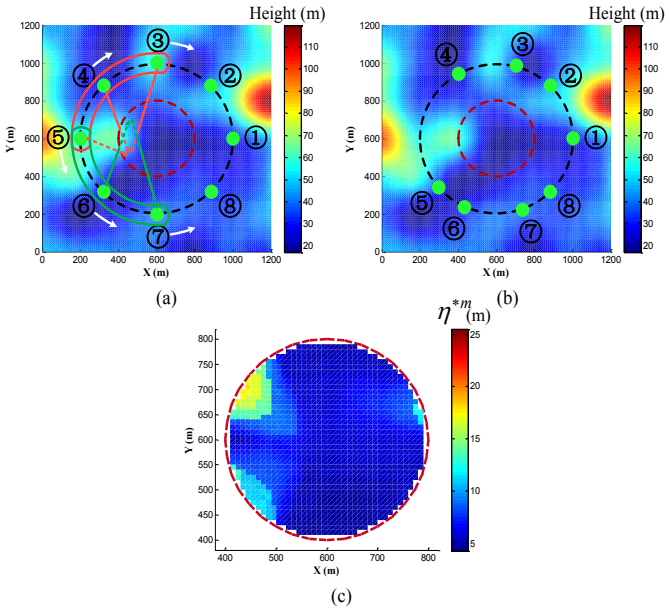

Fig. 12. Example of reliability enhancement: (a) Guidance for SP location adjustment, (b) adjusted SPs, and (c) the enhancement results (η^{*m}).

of SPs 3 and 4. Thus, in order to improve the visibility of these two SPs in hazardous area 1, we rotate them clockwise around the center of the location uncertain area by appropriate angles, as shown in Fig. 12(a). Similarly, we rotate SPs 6 and 7 counterclockwise to improve their visibility in hazardous area 2. Since SP 5 affects the reliability of both areas, the adjustment of its location is the most complicated. To make matter worse, the two hazardous areas have conflicting requirements for the adjustment of SP 5. For example, rotating SP 5 clockwise could reduce its conditional failure rate in hazardous area 1, but at the same time further degrade its visibility in hazardous area 2. It is noteworthy that the cause analysis results shown in Table IV can also help us solve this problem. It can be seen from Table IV, SP 5 has good visibility but high conditional failure rate in hazardous area 2. For this type of SPs, in addition to reducing its conditional failure rate, greatly reducing its visibility to make it almost unavailable is also a potential way to reduce its impact on reliability. Therefore, we rotate SP 5 counterclockwise to improve and

TABLE V
SIMULATION PARAMETERS

Parameter	Value
Main frequency (f_c)	1.5 GHz
Path loss exponent (PLE) in NLoS (α_N)	3.4
Standard deviation of shadowing (σ_N)	1.4 dB
Transmission power of user device ($P_{t,U}$)	20 dBm
Noise power (P_{n_0})	-104 dBm
Standard deviation of terrain uncertainty (σ_h)	1 m
Radius of location uncertainty area (R_{Un})	200 m
Number of sample points (M)	1257 (interval 10m)
Number of service points (SPs) (K)	8
UAV altitude (h_B)	100 m
Minimum horizontal distance between SP and the center of location uncertainty area ($d_{\min}$)	400 m
Response delay of TWR (τ_D)	5 ms
Crystal tolerance of user's oscillator (O_U)	10 ppm
Prior probability of internal fault (P_{IF})	10^{-6}
Tolerable limit of position error (η_{REQ})	20 m
Tolerable FA rate (P_{FA}^{REQ})	10^{-4}
Tolerable MD rate (P_{MD}^{REQ})	10^{-6}
Threshold for hazardous areas (η_T)	18 m

reduce its visibility in hazardous area 1 and 2, respectively. The adjusted SP locations and the enhanced reliability prediction results are shown in Fig. 12(b) and (c), respectively.

As can be seen from Fig. 12(c), the enhanced reliability meets the mission's requirement ($\eta^{*m} < \eta_{REQ} = 20\text{m}$). Numerically speaking, the minimum detectable error after reliability enhancement is 18.06m, which is about 29% less than the original error of 25.50m. These phenomena demonstrate the effectiveness of the proposed voting-based method. Currently, the proposed method only provides guidance for SP adjustment, while the exact locations of adjusted SPs are manually selected according to the guidance. In our future work, we will try to develop a novel reliability enhancement method that could perform SP adjustment automatically.

V. NUMERICAL RESULTS AND DISCUSSION

In this section, a series of simulation experiments are conducted and the corresponding numerical results are provided to verify the applicability of the proposed system, as well as the validity and performance of the proposed methods. Fig. 13 shows a mountainous environment generated with the DEM of realistic terrain, from which we select six test scenarios. The selected scenarios present a varied set of terrains including valleys, peaks and ridges, which could be sufficient to test the repeatability and robustness of the proposed system and methods in different environments. Among them, scenario 3 has been used in the previous section, and the remaining five scenarios will be used for experiments in this section.

In the following subsections, we first apply the proposed UAV-enabled positioning system in all six test scenarios and

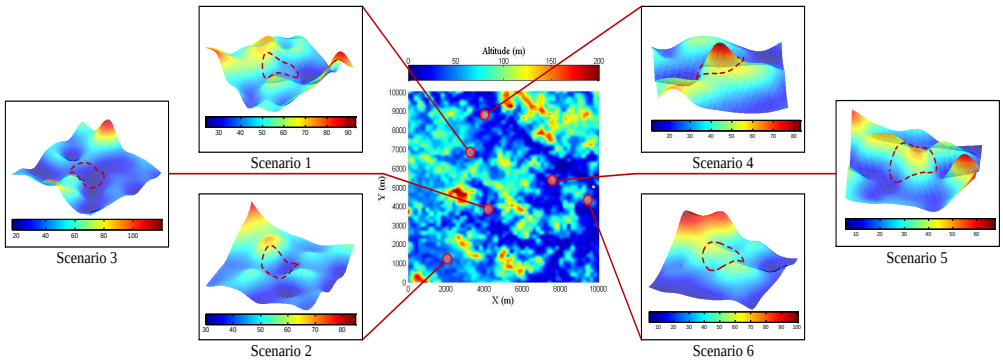

Fig. 13. Test scenarios: Scenarios 1, 2 and 3 present valley environments; scenario 4 presents a mountain peak environment; scenarios 5 and 6 present ridge environments.

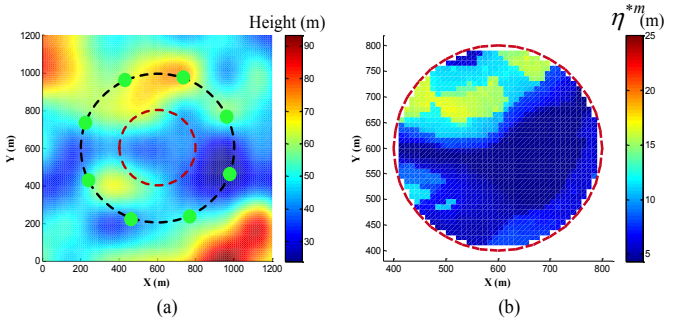

Fig. 14. Reliability prediction in scenario 1: (a) Top view of test scenario 1 and (b) the corresponding prediction results (η^{*m}).

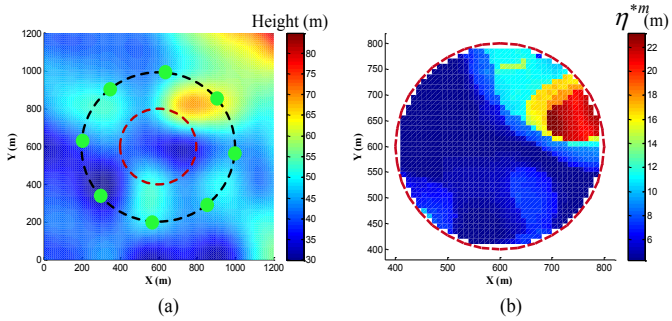

Fig. 15. Reliability prediction in scenario 2: (a) Top view of test scenario 2 and (b) the corresponding prediction results (η^{*m}).

use the reliability prediction method to test its service reliability, so as to illustrate the applicability of our system in different environments. Then, to prove the superiority of the proposed reliability prediction method in mountainous environments, we quantitatively compare it with the widely used LS-RAIM technique in scenarios 1, 4 and 6 [34]. Moreover, quantitative analysis of the key factors affecting the reliability prediction results and their sensitivity is carried out to improve the practicality of our proposed method. Finally, the effectiveness of the proposed voting-based method for reliability enhancement is demonstrated via an experiment conducted in scenario 2. Table V summarizes the key simulation parameters used in this section.

A. Applicability Test of the Proposed System

In this subsection, to demonstrate the applicability of the proposed UAV-enabled positioning system in different environments, we apply it to the six scenarios shown in Fig. 13 and utilize the reliability prediction method introduced in Section III to evaluate its service reliability. Except for the scenario 3 that has already been discussed in Section IV, the reliability prediction results obtained in the remaining five scenarios are shown in Fig. 14 to Fig. 18.

As can be seen from Fig. 14(a), scenario 1 presents a typical situation in mountainous environments where a user is located in a valley surrounded by mountains. This scenario is considered to be very challenging for conventional GNSS systems or terrestrial cellular-based positioning technologies, because their signals are very likely to be blocked by terrain. As shown in Fig. 14(b), in such a challenging scenario, the proposed system could effectively detect failures that cause a position error larger than 16.8m. Moreover, the predicted detectable errors of most sample points in the location uncertainty area are quite small, and only a few sample points have errors larger than 10m. Careful observation reveals that these sample points with large detectable errors form an arc around the mountain. This phenomenon is consistent with intuitive experience, that is, the sample points at the foot of a mountain commonly correspond to poor service reliability because the signal from the other side of the mountain is often blocked. Scenario 2 shown in Fig. 15(a) presents another valley environment and its corresponding reliability prediction results are shown in Fig. 15(b). It can be seen that the predicted minimum detectable position error of the proposed system in this scenario is 23.2m. Similar to the phenomenon observed in scenario 1, the hazardous area formed by sample points with large detectable errors in scenario 2 is also located at the foot of a mountain. Based on the results obtained in scenarios 1 and 2, it can be concluded that the proposed system could work efficiently in valley environments, and the hazardous areas in such environments are commonly located at the foot of mountains.

As shown in Fig. 16(a), the location uncertainty area in scenario 4 covers the top of a mountain and its surrounding slopes, which can be regarded as a typical mountain peak environment. The service reliability of the proposed system

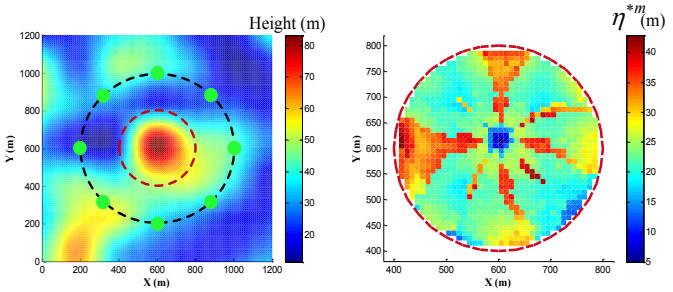

Fig. 16. Reliability prediction in scenario 4: (a) Top view of test scenario 4 and (b) the corresponding prediction results (η^{*m}).

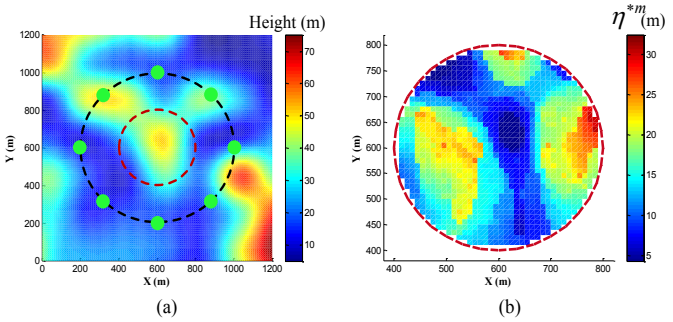

Fig. 17. Reliability prediction in scenario 5: (a) Top view of test scenario 5 and (b) the corresponding prediction results (η^{*m}).

in scenario 4 is shown in Fig. 16(b). It can be observed that in this scenario, the minimum position error that can be detected by the proposed system is 42.8m, which is much worse than that obtained in valley environments. Moreover, it is noteworthy that the service reliability at the top of the mountain is actually acceptable (below 10m), while the sample points with large errors mainly located on the surrounding slopes. Since the top of the mountain has an open sky view while the users on the slopes cannot establish LoS links with UAV behind the mountain, the above phenomenon is reasonable and common in practical applications. According to the above analysis, the proposed system is also applicable to mountain peak environments. Although the service reliability in this type of environments is still somewhat unsatisfactory, it is caused by the complex terrain rather than the proposed system.

Finally, we focus on scenarios 5 and 6 shown in Fig. 17(a) and Fig. 18(a). In both of these two scenarios, there is a ridge running through the location uncertainty area, making them typical examples of ridge environments. Fig. 17(b) and Fig. 18(b) show the reliability prediction results obtained in scenarios 5 and 6, respectively. The minimum detectable errors of the proposed system in these two scenarios are 32.4m and 33.9m, respectively. In addition, it can be observed in both scenarios that most of the sample points on the ridge have relatively good service reliability, while those with large errors are located on both sides of the ridge and clustered into two hazardous areas. The cause of this phenomenon is similar to those explained in the above paragraphs, that is, the signal blockage caused by terrain. The above results indicate that the

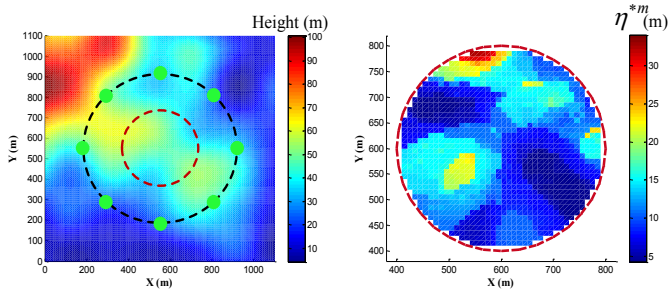

Fig. 18. Reliability prediction in scenario 6: (a) Top view of test scenario 6 and (b) the corresponding prediction results (η^{*m}).

proposed system is capable of operating in ridge environments.

The experimental results discussed above indicate that the proposed UAV-enabled positioning system can work efficiently in different terrains including valleys, peaks and ridges, which demonstrate the applicability of our system in mountainous environments.

B. Performance Comparison of the Proposed Reliability Prediction Method and Existing LS-RAIM Technique

As introduced in Section III, in this article, we propose a reliability prediction method to evaluate the service reliability of the proposed UAV-enabled positioning system. Compared with the existing online fault detection or reliability evaluation methods, the main advantage of the proposed method is that it utilizes the DEM of the realistic terrain to obtain the prior probabilities of signal blockage and NLoS propagation, so that it has the ability to perform offline reliability prediction before the UAV takes off.

In this subsection, to demonstrate the superior performance of the proposed method in mountainous environments, we successively apply it and the well-known LS-RAIM technique in scenarios 1, 4 and 6, and compare their performance in different terrains. It is worth noting that LS-RAIM is an online fault detection method, which needs to know the visibility of anchor nodes before evaluating the service reliability. Besides, in order to deal with multiple simultaneous faults, LS-RAIM also requires the knowledge of the prior probability of each fault, which is commonly set to a small constant in GNSS applications. To compare the proposed method with the LS-RAIM technique under the same conditions, we set parameters P^m_{k,No_LoS} and $P^m_{k,NLoS}$ to constants 10^{-8} and 10^{-9} when using LS-RAIM, thereby extending it to offline reliability prediction.

In each scenario, the proposed method and the LS-RAIM technique were successively used to calculate the minimum detectable error (η^{*m}) at the center of the location uncertainty area and decision threshold (T_g) corresponding to each observation event. Then, a series of Monte-Carlo simulations are carried out to test the reliability prediction results obtained by the above two methods. During each simulation, we randomly specify the visibility and status of each SP according to the corresponding prior probabilities, and generate range measurements based on the model of service failure introduced

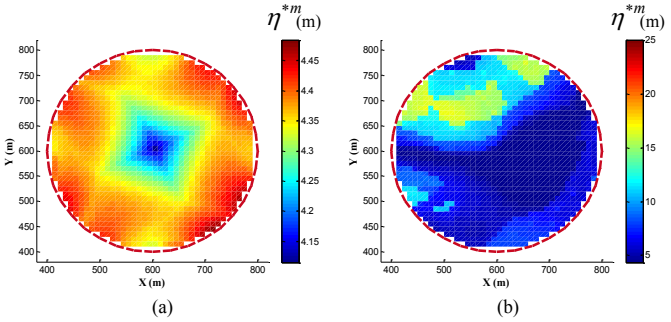

Fig. 19. Performance comparison in scenario 1: Reliability prediction results (η^{*m}) obtained by (a) LS-RAIM and (b) the proposed method.

TABLE VI
PERFORMANCE TEST RESULTS IN SCENARIO 1

	$\eta^*(m)$	FA rate	MD rate
LS-RAIM	4.115	1.147×10^{-4}	1.900×10^{-7}
The proposed method	4.445	9.795×10^{-5}	1.200×10^{-7}

in Section II.B. After the range measurements are generated, both methods perform failure detection based on their decision threshold, and the corresponding FA and MD rates are counted according to the definitions in equations (26) and (31). Since the tolerable FA and MD rates are 10^{-4} and 10^{-6}, the number of Monte-Carlo simulations is set as 10^8 to make the test results statistically significant. The experimental results obtained by Monte-Carlo simulations in three scenarios are shown in Fig. 19 to Fig. 21 and Table VI to Table VIII.

Fig. 19 shows the reliability prediction results obtained by the two methods in scenario 1. It can be seen that at the center of the location uncertainty area, the minimum detectable errors corresponding to the proposed method and LS-RAIM technique are 4.445m and 4.115m, respectively. The reason why the prediction results of the two methods are not much different is that the center of scenario 1 has a clear view of sky, thus the prior probabilities of service failures depend mainly on the probability of internal fault, which is the same between the two methods. Although the reliability prediction results seem to be relatively close, the Monte-Carlo simulation results shown in Table VI highlight the superiority of the proposed method over the existing LS-RAIM technique. It can be seen that the FA and MD rates of the proposed method in this scenario are 9.795×10^{-5} and 1.200×10^{-7}, which meet the mission requirements shown in Table V. The obtained FA rate is slightly lower than the required one, indicating the correctness of the FA rate allocation scheme and threshold setting principle introduced in Section III.C. Moreover, since we consider the worst fault condition when calculating the detectable error, it is not surprising that the obtained MD rate is much lower than the required one. Compared with the satisfactory performance of the proposed method, the simulation results of the LS-RAIM technique are somewhat disappointing. As can be seen from Table VI, the FA and MD rates of LS-RAIM obtained in scenario 1 are 1.147×10^{-4} and 1.900×10^{-7}, respectively. The FA rate of LS-RAIM exceeds the limit, which may have a serious impact on missions that require high service continuity. Although the LS-RAIM's MD rate meets the requirement, it is still much worse than that of the proposed method. Numerically speaking, the MD rate of the proposed method in this scenario is about 36.8% lower than that of the LS-RAIM technique. Based on the above experimental results, it can be concluded that the prediction accuracy of the proposed reliability prediction method is better than that of the existing LS-RAIM technique in scenario 1.

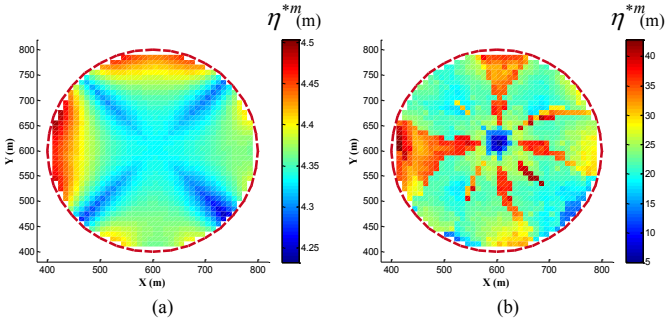

Fig. 20. Performance comparison in scenario 4: Reliability prediction results (η^{*m}) obtained by (a) LS-RAIM and (b) the proposed method.

TABLE VII
PERFORMANCE TEST RESULTS IN SCENARIO 4

	$\eta^*(m)$	FA rate	MD rate
LS-RAIM	4.333	1.274×10^{-3}	5.250×10^{-6}
The proposed method	7.977	9.754×10^{-5}	2.000×10^{-8}

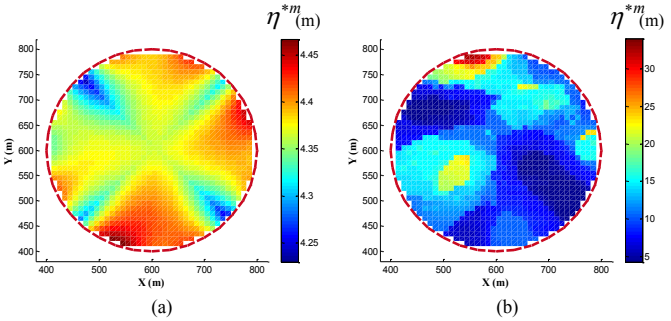

Fig. 21. Performance comparison in scenario 6: Reliability prediction results (η^{*m}) obtained by (a) LS-RAIM and (b) the proposed method.

TABLE VIII
PERFORMANCE TEST RESULTS IN SCENARIO 6

	$\eta^*(m)$	FA rate	MD rate
LS-RAIM	4.364	6.484×10^{-4}	2.044×10^{-5}
The proposed method	8.543	8.522×10^{-5}	2.000×10^{-8}

Fig. 20 shows the reliability prediction results obtain by the two methods in scenario 4, and the corresponding Monte-Carlo simulation results are shown in Table VII. The minimum detectable error of the proposed method at the center of location uncertainty area is 7.977m, which is quite different from the 4.333m obtained by the LS-RAIM technique. Although it seems that LS-RAIM can detect smaller position errors than the proposed method, Monte-Carlo simulations contradict this view. As can be seen from Table VII, the FA and MD rates of

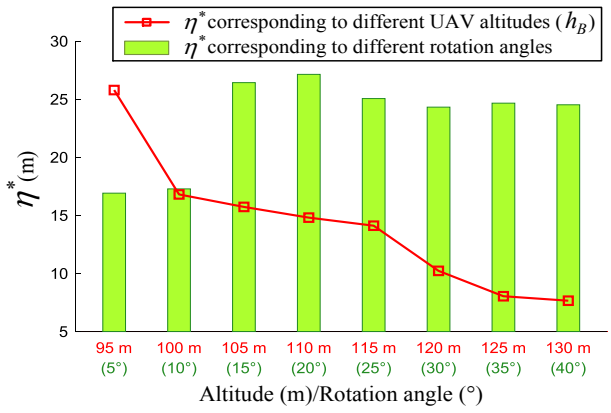

Fig. 22. Analysis of key factors affecting reliability: UAV altitudes and horizontal locations.

LS-RAIM in scenario 4 are 1.274×10^{-3} and 5.250×10^{-6}, which far exceed the corresponding tolerable limits. Thus, the service reliability predicted by LS-RAIM is inaccurate and may mislead the system operator. On the contrary, the FA and MD rates of the proposed method are 9.754×10^{-5} and 2.000×10^{-8}, which meet the mission requirements. In particular, the MD rate of the proposed method in scenario 4 is only about 0.381% of that of the LS-RAIM technique. Therefore, in this scenario, only the proposed method can accurately predict the service reliability of the proposed system, while the LS-RAIM technique is untrustworthy.

Finally, we test and compare the two methods in scenario 6, and the obtained experimental results are shown in Fig. 21 and Table VIII. The service reliability predicted by the proposed method and LS-RAIM are 8.543m and 4.364m, respectively. Although the prediction result of LS-RAIM is smaller, its FA and MD rates are 6.484×10^{-4} and 2.044×10^{-5}, both exceeding the tolerable limits. In contrast, the FA and MD rates of the proposed method both meet the requirements. In particular, the MD rate of the proposed method in this scenario is only about 0.0978% of that of the LS-RAIM technique. Therefore, in scenario 6, the proposed method also exhibits prediction accuracy far superior to the existing LS-RAIM technique.

It can be seen from the above experimental results that in scenarios 1, 4 and 6, the MD rate of the proposed method is at least 36.8% lower than that of the existing LS-RAIM technique. Since the three scenarios used in simulations represent three typical terrains and the proposed method outperforms the LS-RAIM technique in these scenarios, we believe that the experimental results analyzed above are sufficient to demonstrate the superior performance of the proposed reliability prediction method in mountainous environments.

C. Key Factors Affecting the Service Reliability

With the reliability prediction method introduced in Section III, we can predict the service reliability of the proposed UAV-enabled positioning system in a specified mountainous environment. Then, in this subsection, we further analyze the key factors affecting the reliability of the proposed system.

We first study the influence of the UAV altitude on service reliability through a simulation experiment in scenario 1. During the experiment, the SPs are deployed at the same horizontal locations as shown in Fig. 14(a), and the parameters other than the UAV altitude are set according to Table V and remain unchanged. The altitude of UAV platform increases from 95 to 130m at an interval of 5m, and the minimum detectable error corresponding to each altitude is calculated with the proposed reliability prediction method. The red line in Fig. 22 shows the variation of the predicted reliability with the UAV altitude. It can be seen clearly that the reliability improves as the altitude increases. This phenomenon is quite easy to understand since the increase in altitude leads to better visibility as well as a smaller NLoS probability, which ultimately results in better reliability. Numerically speaking, the detectable error obtained at the altitude of 130m is 7.654m, which is only about 30% of the 25.79m obtained at 95m. The average reduction of the detectable error brought about by a 5m increase in UAV altitude in scenario 1 is about 15%. Moreover, the improvement of service reliability brought about by increasing altitude is related to the current altitude of the UAV platform. At the altitude of 95m, an increase of 5m in altitude could reduce the minimum detectable error by more than 35%. If the current altitude is between 100m and 115m, the increase of UAV altitude has a similar but relatively weaker effect on service reliability, with an average improvement of 5.6% brought about by a 5m increase in altitude. Therefore, in practical applications, the decision to increase UAV altitude should be made carefully after considering factors such as the current altitude and the energy consumption required for altitude changes.

Moreover, we also conduct an experiment to investigate how the SPs' locations affect service reliability. During the experiment, the altitude of UAV platform is set to 100m and remains constant. Then, we change the locations of SPs by rotating all of them counterclockwise at the same time. The bar chart in Fig. 22 shows the reliability prediction results obtained at different rotation angles. It can be seen that in scenario 1, with the increase of rotation angle, the predicted minimum detectable error first increases and then decreases, ranging from 16.8m to 27.1m. The reliability corresponding to the best rotation angle ($5°$) has a 38% improvement compared with that corresponding to the worst rotation angle ($20°$). The above phenomenon indicates that the selection of SPs' locations is also one of the main factors that affect the proposed system's reliability. In addition, optimizing the locations of SPs can improve the service reliability without changing the UAV altitude, which is an important basis for reliability enhancement.

As discussed in Appendix A, the range measurement noise in the proposed system is dominated by the clock drift error, whose variance (σ_C^2) depends on the crystal tolerance of user's oscillator (O_U) and the response delay of TWR (τ_D). Thus, it is obvious that the values of parameters O_U and τ_D are factors that affect the service reliability of the proposed system. Then, another simulation experiment is carried out to analyze the relationship between service reliability and these two parameters. During the experiment, we first increase the

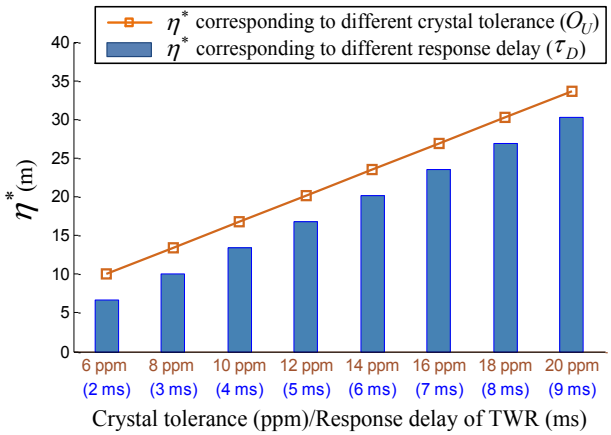

Fig. 23. Analysis of key factors affecting reliability: Crystal tolerance of user's oscillator and response delay of TWR .

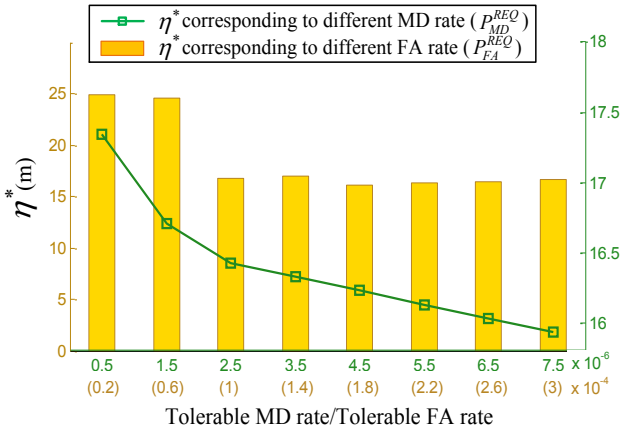

Fig. 24. Analysis of key factors affecting reliability: Tolerable MD and FA rates.

crystal tolerance from 6ppm to 20ppm at an interval of 2ppm, and then gradually increase the response delay from 2ms to 9ms. Note that when the value of a certain parameter changes, the other parameters are set according to Table V and remain unchanged. The brown line and bar chart in Fig. 23 show the minimum detectable errors corresponding to different crystal tolerance and response delay, respectively. It can be seen that the detectable error increases linearly with the increase of O_U and τ_D. These linear relationships are expected and can be explained as follows. According to equation (62) in Appendix A, the standard deviation of clock drift error (σ_C) is linear with O_U and τ_D. Moreover, as will be proved in Appendix D, the minimum detectable error (η^*) has a linear relationship with σ_C. Thus, the linear relationships shown in Fig. 23 are reasonable and not surprising. In terms of the crystal tolerance, the detectable error corresponding to 2ppm is 10.08m, which is only about 30% of the 33.61m corresponding to 20ppm. This phenomenon indicates that as long as the cost is acceptable, equipping user devices with better local clocks can help improve the service reliability of the proposed system. As for the response delay, the detectable error corresponding to 2ms is 6.722m, which is almost 78% lower than the 30.25m corresponding to 9ms. Therefore, appropriately reducing the response delay of TWR is conducive to the improvement of service reliability. However, since the response delay needs to be longer than the packet duration, the improvement of service reliability brought about by reducing the response delay is very limited in practical applications.

According to equations (46)-(48), the calculation of minimum detectable error is related to the decision threshold (T_g) and the tolerable MD rate. In addition, as introduced in Section III.C, the setting of the decision threshold mainly depends on the tolerable FA rate. Therefore, the tolerable FA and MD rates are two important factors that affect service reliability. Although these two parameters are commonly set according to mission requirements, we still conduct a simulation experiment to investigate their influence on the proposed system's performance. During the experiment, we first increase the tolerable MD rate from 0.5×10^{-6} to 7.5×10^{-6} at an interval of 1.0×10^{-6}, while keeping the tolerable FA rate as 1.0×10^{-4}. The green line in Fig. 24 shows the minimum detectable errors corresponding to different MD rates. It can be seen clearly that the detectable error decreases with the increase of tolerable MD rate. Fig. 8 in Section III.A can help us understand this phenomenon. It can be seen from Fig. 8 that increasing the tolerable MD rate makes it possible to reduce the non-centrality parameter of the chi-square distribution in failure condition. Moreover, according to equation (48), the minimum detectable error is linear with the square root of the non-centrality parameter. Thus, it is obvious that larger tolerable MD rate will lead to smaller detectable error. Numerically speaking, the service reliability corresponding to MD rate of 7.5×10^{-6} is 15.93m, which is about 8.1% lower than the 17.34m corresponding to MD rate of 0.5×10^{-6}. So, the improvement of service reliability brought about by increasing the tolerable MD rate is not significant. Then, we focus on the relationship between service reliability and the tolerable FA rate. During the experiment, the tolerable FA rate increases from 0.2×10^{-4} to 3.0×10^{-4} at an interval of 0.4×10^{-4}, while the tolerable MD rate remains constant as shown in Table V. The service reliability corresponding to different tolerable FA rates is shown as the bar chart in Fig. 24. It can be seen that as the tolerable FA rate increases, the minimum detectable error first decreases, and then fluctuates within a small range. This phenomenon can be explained as follows. According to the equation (32), the decision threshold decreases with the increase of tolerable FA rate. As can be seen from Fig. 8, the decrease of the decision threshold allows the non-centrality parameter of the chi-square distribution to decrease, which will eventually lead to a smaller detectable error. Thus, it is reasonable for the minimum detectable error to decrease at the beginning of the increase of the tolerable FA rate. In addition, as the tolerable FA rate further increases, some observation events that originally need to be considered are now ignored according to equation (37). The occurrence of this situation may change the sample point corresponding to the minimum detectable error, resulting in fluctuations in service reliability. Numerically speaking, the best service reliability during the experiment is 16.13m, which is about 35% lower than the

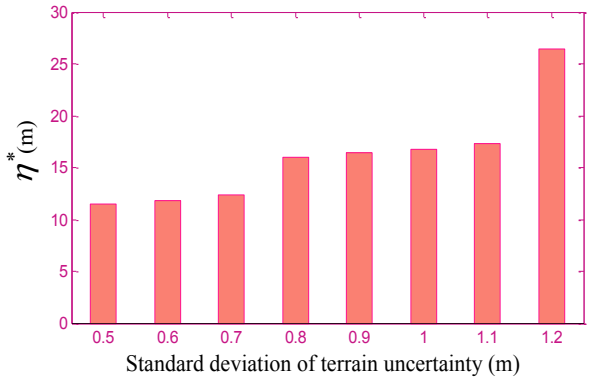

Fig. 25. Analysis of key factors affecting reliability: Standard deviation of terrain uncertainty.

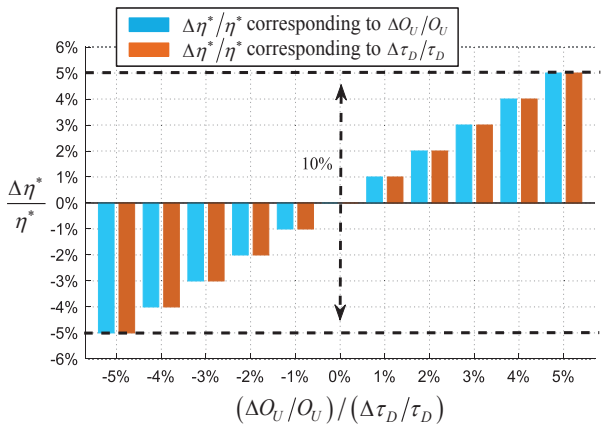

Fig. 26. Sensitivity analysis: Crystal tolerance of and response delay.

worst reliability (24.88m). Based on the above experimental results, it can be concluded that the improvement of service reliability brought about by adjusting tolerable FA and MD rates is not significant. In practical applications, it is better to set these two parameters according to mission requirements.

In the proposed system, the prior probabilities of signal blockage and NLoS propagation are indispensable for reliability prediction. Moreover, as introduced in Section II, the standard deviation of terrain uncertainty (σ_h) is an important parameter in the calculation of these prior probabilities. Therefore, σ_h is certainly one of the key parameters that affect reliability prediction results. To this end, at the end of this subsection, a simulation experiment is carried out to show the variation of service reliability with the standard deviation of terrain uncertainty. During the experiment, the value of σ_h increases from 0.5m to 1.2m at an interval of 0.1m, while the other parameters remain constant as shown in Table V. The bar chart in Fig. 25 shows the predicted minimum detectable error corresponding to different standard deviation of terrain uncertainty. Generally speaking, the service reliability degrades with the increase of terrain uncertainty. Numerically speaking, the detectable error corresponding to the standard deviation of 0.5m is 11.48m, which is almost 57% lower than the 26.41m corresponding to the standard deviation of 1.2m. This phenomenon indicates that accurate terrain information helps to improve the service reliability of the proposed system. Therefore, in practical applications, we should always use the most accurate DEM data we can find.

D. Sensitivity Analysis of Parameters

As can be seen from Table V, the realization of the reliability prediction function in the proposed system requires a lot of parameters. The influences of these parameters on service reliability have already been discussed in the previous subsection. Then, in this subsection, we try to utilize a series of simulation experiments to find out what will be happened to the service reliability with a small change in parameters, that is, the sensitivity of parameters. Among the key factors affecting the service reliability, the altitude of UAV platform and SPs' locations can be precisely controlled by the airborne navigation equipment. Moreover, the tolerable FA and MD rates are set by the system operator according to mission requirements. Thus, in this subsection, we mainly focus on the sensitivity of crystal tolerance, response delay and terrain uncertainty.

In practical applications, user devices commonly use low-cost local clocks, whose actual crystal tolerance may be slightly different from that claimed by the manufacturer. Thus, we first conduct a simulation experiment in scenario 1 to investigate the sensitivity of crystal tolerance with respect to the reliability prediction results. The blue bars in Fig. 26 show the variation of minimum detectable error when there is a small change in crystal tolerance. The abscissa of Fig. 26 represents the ratio of the change of the parameter to its original value. Since the original value of crystal tolerance is set to 10ppm as shown in Table V, its variation in the experiment is within -0.5∼0.5ppm. It can be seen clearly that the change in minimum detectable error has a linear relationship with that in crystal tolerance. This phenomenon has been explained in detail in the previous subsection. Numerically speaking, when the crystal tolerance varies within -5∼5%, the variation of the minimum detectable error does not exceed 10%, which is equivalent to a position error of 1.681m. Moreover, we also test the sensitivity of the response delay, and the corresponding results are shown as the brown bars in Fig. 26. Similar to the crystal tolerance, a small change in response delay will cause a linear variation of the minimum detectable error, and the variation is no more than 10% (1.681m). Since system operators commonly leave a certain margin for potential performance degradations when making decisions, a prediction error of 1.681m rarely has considerable impacts on mission execution. Therefore, performance variations caused by small changes in crystal tolerance or response delay are acceptable in practical applications.

As discussed in the previous subsection, the standard deviation of terrain uncertainty is one of the key factors that affect the proposed system's performance. In practice, the value of parameter σ_C used in reliability prediction commonly represents the standard deviation in the whole area, which may be slightly different from that in a certain local area. Thus, at the end of this subsection, the sensitivity of terrain uncertainty with respect to the reliability prediction results

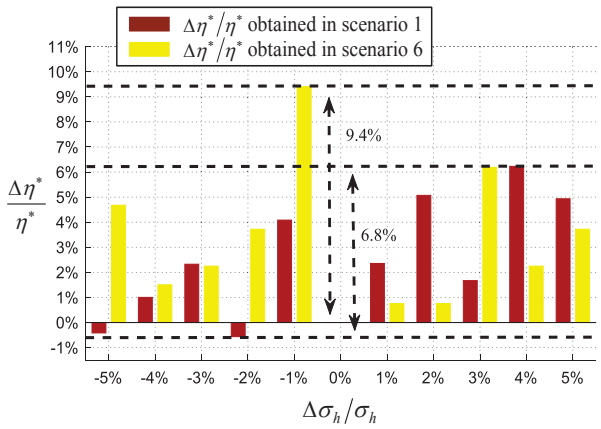

Fig. 27. Sensitivity analysis: Standard deviation of terrain uncertainty.

is analyzed through two simulation experiments in scenarios 1 and 6. The bar chart in Fig. 27 shows the variation of the minimum detectable error caused by small changes in the standard deviation of terrain uncertainty. It can be seen that in both scenarios, the predicted detectable error fluctuates with small changes in σ_C. Therefore, although the service reliability generally improves with the decrease of terrain uncertainty, its changing trend caused by small changes in terrain uncertainty is not fixed. This phenomenon does not contradict the conclusion that using more accurate DEM data helps to improve the service reliability. Numerically speaking, when the standard deviation of terrain uncertainty varies within -5∼5%, the variations of the minimum detectable error in scenarios 1 and 6 are less than 6.8% and 9.4%, which are equivalent to position errors of 1.141m and 3.191m. Based on the above experimental results, we believe that small changes in the standard deviation of terrain uncertainty will not have significant impacts on the proposed system's performance.

E. Validity Test of the Proposed Enhancement Method in Valley Environments

In Section IV, the proposed voting-based cause analysis method for reliability enhancement has been successfully applied in scenario 3, which is a typical valley environment. In this subsection, we test it in scenario 2 to demonstrate its validity in valley environments again. The test scenario and its corresponding reliability prediction results are shown in Fig. 28(a) and (b), respectively. It can be seen that there is a hazardous area in Fig. 28(b). The worst service reliability in this hazardous area is 23.15m, which is almost 16% larger than the tolerable limit of position error. Therefore, without reliability enhancement, the performance of the proposed system in this scenario cannot meet the mission requirements. Then, we use the proposed method to analyze the cause of the hazardous area, and the analysis results are shown in Table IX. The analysis results indicate that the low visibility of SPs 2, 3 and the high conditional failure rate of SP 1 lead to the unsatisfactory reliability of the hazardous area.

Based on the cause analysis results obtained by the proposed method, we adjust the locations of SPs as follows. In order to improve the visibility of SPs 2 and 3, we rotate them

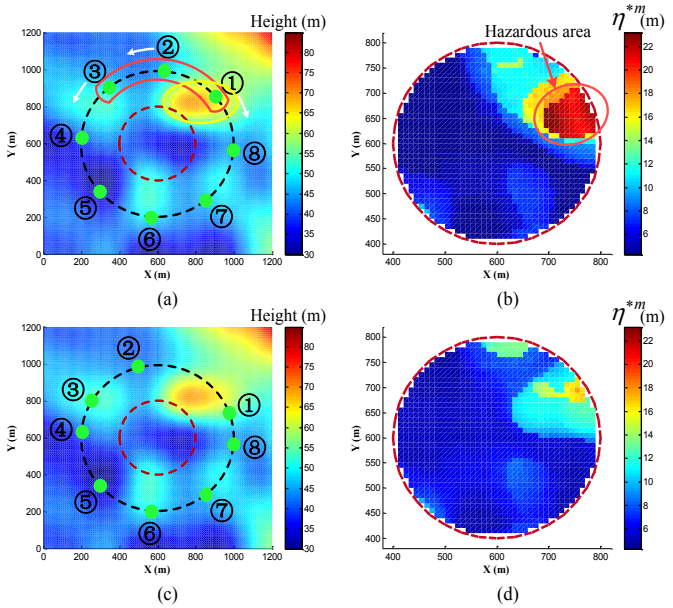

Fig. 28. Reliability prediction and enhancement in scenario 2: (a) Top view of test scenario 2 and (b) the prediction results (η^{*m}), (c) adjusted SPs and (d) the enhancement results (η^{*m}).

TABLE IX
CAUSE ANALYSIS RESULTS IN TEST SCENARIO 2

	SP1	SP2	SP3	SP4	SP5	SP6	SP7	SP8
$\mathbf{v}^{*x}_{H_1,U}$	0	1	1	0	0	0	0	0
$\mathbf{v}^{*x}_{H_1,F\|O}$	1	1	0	0	0	0	0	0
$\mathbf{v}^{*y}_{H_1,U}$	0	1	1	0	0	0	0	0
$\mathbf{v}^{*x}_{H_1,F\|O}$	1	1	0	0	0	0	0	0

counterclockwise by appropriate angles so that their signals are less likely to be blocked by mountains. Then, we rotate SP 1 clockwise to reduce its NLoS probability. The adjusted SP locations and the corresponding enhanced reliability are shown in Fig. 28(c) and (d), respectively. It can be seen that the minimum detectable error after reliability enhancement is 17.90m, which is about 23% less than the original error of 23.15m and meets the mission requirements. Since scenarios 2 and 3 present typical valley environments and the proposed voting-based cause analysis method performs well in these two scenarios, it can be concluded that the proposed method is effective for reliability enhancement in valley environments.

It is noteworthy that although the proposed enhancement method exhibits satisfactory validity in valley environments, it may not be applicable for other types of terrains like peaks and ridges. The reason for this phenomenon is as follows. In valley environments represented by scenarios 2 and 3, the number of hazardous areas is relatively small and the adjustments of SPs' locations for different hazardous areas rarely conflict with each other. In other words, in valley environments, we can often eliminate a certain hazardous area by adjusting some SPs without degrading the service reliability in other hazardous areas. In peak environments and ridge environments represented by scenarios 4 and 5, although the proposed

voting-based method can still be used to analyze the cause of hazardous areas, conflicts exist in the adjustment of SPs' locations. Taking scenario 4 shown in Fig. 16 as an example, there are 7 hazardous areas on the slopes around the top of the mountain. The causes of these hazardous areas are quite similar, that is, the signal blockage and NLoS propagation caused by the mountain peak. However, if we try to eliminate the hazardous areas on the left side of the peak by moving those SPs on the right to the left, the service reliability in the hazardous areas on the right will be further degraded because the number of visible SPs becomes smaller. Similar conflicts can also be found between the two hazardous areas in ridge environments. This kind of conflicts hinders the application of the proposed enhancement method in environments other than valley. Of course, in those environments where the proposed method is not applicable, we can still improve the service reliability of the proposed system by increasing the altitude of the UAV platform.

F. Discussion

In the previous subsections, we presented and analyzed the numerical results obtained through a series of simulation experiments. Then, in this subsection, we evaluate the proposed system and methods based on the obtained numerical results and draw important conclusions.

At the beginning of this section, we successfully applied the proposed system and reliability prediction method in six scenarios, which represent three typical terrains in mountainous environments including valleys, peaks and ridges. Numerical results presented in subsection A show that the proposed method could efficiently predict the service reliability of the proposed system in different environments, and the prediction results are consistent with intuitive experience. Thus, we believe that these numerical results demonstrate the applicability and repeatability of the proposed system and reliability prediction method in mountainous environments.

Then, we quantitatively compared the performance of the proposed reliability prediction method and the existing LS-RAIM technique through Monte-Carlo simulations. The numerical results presented in Table VI-VIII show that the FA and MD rates of the proposed method always meet the requirements, while LS-RAIM does not. Moreover, the MD rate of the proposed system is at least 36.8% lower than that of LS-RAIM. Therefore, compared with the widely used LS-RAIM technique, the proposed method has higher reliability prediction accuracy in mountainous environments.

Moreover, in subsections C and D, we also conducted experiments to analyze the key factors that affect service reliability and their sensitivity. The numerical results presented in Fig. 26 and Fig. 27 show that the variation of the proposed system's service reliability caused by small changes in parameters does not exceed 10%. Thus, the proposed system and reliability prediction method are robust to small changes in parameters.

Finally, the validity of the proposed voting-based cause analysis method for reliability enhancement was tested and its limitations were analyzed in detail. The numerical results show that the proposed method reduces the minimum detectable errors in the two valley scenarios by 23% and 29%, respectively. Therefore, the proposed method could effectively enhance the service reliability of the proposed system in valley environments.

The numerical results and the above discussions demonstrate that the proposed system is applicable to different mountainous environments and the corresponding reliability prediction method performs better than the existing technique. In addition, the service reliability of our system is robust to small changes in parameters and can be further enhanced in certain environments. Therefore, we believe that the proposed system has strong potential for providing reliable positioning services in mountainous environments.

VI. Threats to Validity

The proposed UAV-enabled positioning system and the corresponding methods for reliable positioning have been introduced and tested above. It is worth noting that in practice, the validity of our system or methods may be threatened by some issues. For this reason, this section explains the delimitation of the proposed system and methods by describing possible threats to validity. In the following paragraphs, we focus on five types of threats and discuss them in detail.

- *Construct validity*: the design of a system and the methods used in it is closely related to the definition of the key performance metric. In this article, the service reliability is chosen as the performance metric for our UAV-enabled positioning system, and is defined as the minimum detectable position error. The Monte-Carlo simulations in Section V.B demonstrate that the detectable errors calculated by the proposed method accurately reflect the service reliability of the proposed system. Of course, the minimum detectable error is definitely not the only choice for measuring the reliability of positioning services. If the definition of service reliability changes, both methods proposed in this article may need to be redesigned. The above issues are classified as threats to construct validity.
- *Internal validity*: the parameter setting in a system will undoubtedly affect the performance. Experimental results presented in Section V.C show that the key factors affecting our system's performance include UAV altitude, SPs' horizontal locations, crystal tolerance of user's oscillator, response delay of TWR and the standard deviation of terrain uncertainty. The experiments conducted in Section V.D demonstrate that small changes in these parameters will not cause significant impacts on performance. However, if a certain parameter deviates a lot from its actual value, the performance and validity of the proposed system will certainly be affected. Therefore, in practical applications, system operators should ensure the accuracy of parameter setting.
- *External validity*: in terms of the generalization ability of the proposed system and methods in the real world, we have tested them in scenarios generated with the DEM of realistic terrain. The test scenarios present three typical terrains in mountainous environments, namely valleys, peaks and ridges. It is noteworthy that in practical applications, the proposed system may be deployed in more

challenging environments than those described above, such as caves and cliffs. Moreover, in this article, the UAV platform is assumed to be able to hover stably at each SP. In practice, environment factors like wind may cause the UAV to deviate from the preset SPs. The above issues may affect the generalization of this study in the real world, and need to be studied in future work.

- *Conclusion validity*: the major issue that could affect the conclusion validity of this article is the number of test scenarios. Limited by the length of the article and the time complexity of Monte-Carlo simulations, the number of test scenarios is set to six. Although the numerical results obtained in Section V illustrate that it is promising to design reliable positioning systems with UAV platforms, we acknowledge that the scenarios used in experiments cannot represent all the terrains that exist in mountainous environments. We are aware of this limitation, and only regard this article as the preliminary findings for further studies. In future work, we will try to test the proposed system in more scenarios with complex terrains.
- *Reliability*: one of the issues that affect the repeatability of this study is the DEM resolution. The resolution of DEM data used in this article is 10m, in other words, the horizontal distance between two adjacent DEM data points is 10m. Considering that researchers could have different DEM data sources, difference in resolution will lead to different experimental results. In addition, in this article, we use the TWR-based method to provide positioning services, in which the measurement noise is dominated by the clock drift error. If other researchers adopt different positioning methods like TDoA, different results will occur due to the different forms of measurement noise. Therefore, although the methodology used in this article is general, difference in models or parameters will cause changes in experimental results.

VII. Conclusion

In this article, we proposed a novel UAV-enabled positioning system for providing highly reliable positioning services in mountainous environments. We first designed the structure and operation scheme of the system, and selected the appropriate method to support positioning service. Then, the major causes of service failures were theoretically analyzed, and a failure model was established to describe their prior probabilities and impacts on positioning performance. Based on the established failure model, we proposed a reliability prediction method to evaluate the reliability of the positioning service before the UAV takes off. Moreover, for those situations where the predicted reliability fails to meet the requirements, we also proposed a voting-based method to analyze the causes of unsatisfactory reliability and provide guidance for reliability enhancement. Numerical results demonstrated the strong potential of our system for reliable positioning, as well as the effectiveness of the proposed methods. We hope that this article would bring inspiration for the application of UAVs in future networks and lead to a new practical solution for reliable positioning service.

VIII. Future Work

This article presents the preliminary progress we have made in designing a reliable UAV-enabled positioning system for mountainous environments. The proposed reliability prediction and enhancement methods enable the system operators to predict the reliability of positioning services before the UAV takes off, and enhance it in certain environments. However, the proposed methods still have some limitations, which should be eliminated in the future. Moreover, offline reliability prediction is only one of the functions that a reliable positioning system should support, and there are many other functions that need to be studied and realized. Thus, we still have a long way to go to achieve our goal of reliable positioning.

In the following subsections, we list three important aspects recommended for future work.

A. Improvement of the Reliability Enhancement Method

In the Section IV of this article, we proposed a voting-based method to analyze the causes of hazardous areas and enhance the service reliability, whose effectiveness in valley environments has been verified through simulation experiments. So far, the proposed method only provides rough guidance for the adjustment of SPs' locations, while the exact locations of adjusted SPs are manually selected. In practical applications, it is obviously unrealistic for system operators to manually adjust SPs one by one. Thus, in order to improve the practicability of the proposed system, it is necessary to develop novel reliability enhancement methods with a higher degree of automation.

Moreover, as discussed in Section V.E, the validity of the proposed enhancement method is somewhat unsatisfactory in environments other than valleys. One of the reasons for this phenomenon is that the proposed method only adjusts the azimuth of SPs, but ignores the adjustments of SPs' horizontal distance and altitude. Future enhancement methods should be able to automatically adjust the horizontal location and altitude of each SP to effectively improve the reliability of the proposed system in any terrain environment.

B. Design of Online Reliability Evaluation Methods

In a reliable UAV-enabled positioning system, the offline reliability prediction method should be used in conjunction with the online reliability evaluation method. The former predicts the detectable service failures before the UAV takes off, while the latter is responsible for evaluating the reliability of the positioning results in real time during the mission. Since the reliability prediction has been studied in this article, we recommend for future work designing online reliability evaluation methods for UAV-enabled positioning.

Failure detection and exclusion are two basic functions that an online reliability evaluation method should support. During the mission, the failure detection function analyzes the obtained range measurements to detect service failures that cause position errors larger than the tolerable limit. Then, after a service failure is detected, the failure exclusion function will be used to identify and remove the faulty measurements, and re-evaluate the service reliability of the remaining measurements. Different from the existing fault detection methods

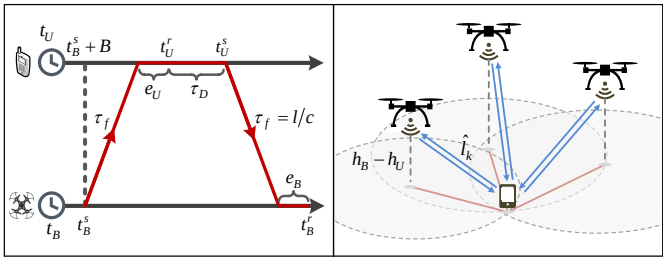

(a) (b)

Fig. 29. Model of TWR-based positioning: (a) Time diagram of TWR and its (b) application example.

originally developed for GNSS applications, the future online reliability evaluation methods for UAV-enabled positioning should consider the NLoS propagation caused by complex terrains as the main source of service failures. Moreover, the DEM data that plays an important role in this article can also be used for online reliability evaluation to improve the accuracy of failure detection and the speed of failure exclusion.

C. Design of Online Reliability Maintenance Strategies

The performance of a reliable positioning system should always meet the mission requirements. Thus, once a failure is detected and the performance after failure exclusion still fails to meet the requirements, measures should be taken according to certain strategies to maintain the service reliability within an acceptable range. Since service failures cannot be completely avoided in practical applications, it is necessary to design online reliability maintenance strategies for UAV-enabled positioning in future work.

One of the basic strategies for reliability maintenance is to add new SPs. The number and locations of these new SPs should be selected carefully. Many factors need to be taken into consideration in location selection, including visibility, the prior probabilities of NLoS propagation and the geometry between the new SPs and the existing uncontaminated SPs. In addition, the positioning result obtained after failure exclusion may not be reliable enough, but can be used to reduce the size of the location uncertainty area. Thus, the design of reliability maintenance strategies should make full use of the location information provided by existing range measurements.

APPENDIX A
MODEL OF TWR-BASED POSITIONING

In the proposed system, TWR-based positioning is selected to support the positioning service. Compared with the OTDoA positioning widely used in terrestrial cellular networks, TWR-based positioning eases the constraint of time synchronization between anchor nodes, making it suitable for single-UAV systems [54]. In TWR-based positioning, the time of flight (ToF) τ_f is obtained through an exchange of messages between the UAV platform and the ground user, as shown in Fig. 29(a). Specifically, the UAV platform first sends a ranging request message to the user device at local time t_B^s. Since the local clocks on both sides are not tightly synchronized in advance, the user device has an unknown clock bias B with respect to the UAV platform at the beginning of the session. Moreover, the clock drift caused by the limited performance of internal oscillator exists in both local clocks, which affects the accuracy of the time interval measurement. The clock drifts of the UAV platform and the user device relative to the perfect clock are denoted by δ_B and δ_U, respectively. After $\tau_f = l/c$ seconds of propagation, the request message arrives at the user device and is detected at user's local time t_U^r, which can be expressed as

$$t_U^r = t_B^s + B + \tau_f\,(1+\delta_U) + e_U, \tag{54}$$

where e_U is the time of arrival (ToA) measurement error caused by the device's internal noise.

After receiving the request message, the user device waits for a fixed time τ_D according to its own local clock, and then sends back a response message at local time

$$t_U^s = t_U^r + \tau_D. \tag{55}$$

Finally, the response message is detected by the UAV platform at local time t_B^r, which can be expressed as

$$t_B^r = t_B^s + 2\tau_f\,(1+\delta_B) + (e_U+\tau_D)\cdot\frac{(1+\delta_B)}{(1+\delta_U)} + e_B. \tag{56}$$

After receiving the response message, the UAV platform can estimate the ToF according to its local clock, and the estimated value $\hat{\tau}_f$ is given by

$$\begin{aligned}\hat{\tau}_f &= \frac{1}{2}\left[(t_B^r - t_B^s) - (t_U^s - t_U^r)\right] \\ &= \tau_f\,(1+\delta_B) + \frac{\tau_D\,(\delta_B-\delta_U)+e_U\,(1+\delta_B)}{2\,(1+\delta_U)} + \frac{e_B}{2}.\end{aligned} \tag{57}$$

The ToF estimation error can be expressed as

$$\hat{\tau}_f - \tau_f = \tau_f\delta_B + \frac{\tau_D\,(\delta_B-\delta_U)+e_U\,(1+\delta_B)}{2\,(1+\delta_U)} + \frac{e_B}{2}. \tag{58}$$

Note that the ToF is typically much smaller than the response delay ($\tau_f \ll \tau_D$), because the latter includes not only the turnaround time between the transmit and receive modes but also the packet duration of several milliseconds [55]. Besides, we assume that the airborne transceiver is equipped with a high-performance oscillator. Thus, the clock drift of the UAV platform is negligible relative to that of the user's low-cost device, that is, $\delta_B \ll \delta_U \ll 1$. Then, the expression of ToF estimation error can be rewritten as

$$\hat{\tau}_f - \tau_f \approx -\frac{\tau_D\delta_U}{2} + \frac{e_U}{2} + \frac{e_B}{2}. \tag{59}$$

Under normal conditions where the NLoS propagation phenomenon and internal faults do not exist, the 3-D distance can be obtained from the estimated ToF utilizing the relationship $\hat{l} = \hat{\tau}_f \cdot c$. The corresponding ranging error can be expressed as

$$\Delta\hat{l} = c\,(\hat{\tau}_f - \tau_f) = n_C + n_U + n_B, \tag{60}$$

where $n_C = -(c\cdot\tau_D\delta_U)/2$ denotes the clock drift error; $n_U = (c\cdot e_U)/2$ and $n_B = (c\cdot e_B)/2$ are ranging errors caused by internal noise of the user device and the UAV platform, respectively. Without loss of generality, we model

the clock drift error as a noise component, which follows a zero-mean Gaussian distribution:

$$n_C \sim \mathcal{N}\left(0, \sigma_C^2\right), \tag{61}$$

where σ_C^2 denotes the variance of the clock drift error. The reason for modeling the clock drift error as the Gaussian noise shown in equation (61) is that without the prior knowledge of observation noise, the Gaussian noise model commonly corresponds to the worst performance of an estimator and is therefore suitable for reliability evaluation [56]. If the crystal tolerance of user's oscillator O_U is known, the value of parameter σ_C^2 can be determined using the following equation:

$$\sigma_C^2 = \left(\frac{c \cdot \tau_D}{2}\right)^2 \cdot \left(\frac{O_U}{3}\right)^2 = \left(\frac{c \cdot \tau_D O_U}{6}\right)^2. \tag{62}$$

The other two terms on the right-hand side of equation (60) are also Gaussian noise components, that is, $n_U \sim \mathcal{N}\left(0, \sigma_U^2\right)$ and $n_B \sim \mathcal{N}\left(0, \sigma_B^2\right)$. In practice, the influence of devices' internal noise on ranging performance is typically negligible relative to the clock drift error [52], that is, $\sigma_U^2 \ll \sigma_C^2$, $\sigma_B^2 \ll \sigma_C^2$. Therefore, the expression of range measurement noise for TWR can be approximated as

$$\Delta\hat{l} = n_C + n_U + n_B \approx n_C. \tag{63}$$

From the above analysis, it can be seen that the range measurement noise of TWR depends mainly on the user's clock drift, whose variance is known and remains constant during the mission. As will be explained in Section III, this characteristic is very important for the detection of service failures.

As shown in Fig. 29(b), after the UAV platform traverses all SPs and performs TWR, the ground user's location can be estimated by solving the following equations:

$$\hat{l}_k = \sqrt{(h_B - h_U)^2 + \|\mathbf{w}_k - \mathbf{u}\|^2} + n_C, \quad k \in \mathcal{K}, \tag{64}$$

where $\hat{l}_k$ is the range measurement obtained at the k-th SP; $\mathbf{u}$ and h_U denote the user's horizontal coordinate and altitude, respectively. As mentioned at the beginning of Section II, each user device is equipped with a barometer. During the TWR process, the accurate altitude measured by the barometer would be contained in the response message and sent to the UAV platform. Thus, only the horizontal coordinate $\mathbf{u}$ needs to be estimated, that is to say, the localization problem studied in this article is still a 2-D localization problem. In addition, when predicting the service reliability, the altitude of each sample point h_U^m is set as the sum of the corresponding DEM data and the average height of handheld devices (1.5m).

APPENDIX B
PSEUDOCODE FOR THE PROPOSED RELIABILITY PREDICTION METHOD

Algorithm 1 Proposed Reliability Prediction Method

Input: DEM of realistic terrain, coordinate of each SP ($\mathbf{w}_k$, h_B), number of sample points M, coordinate of each sample point ($\mathbf{u}_m$, h_U^m), tolerable FA rate P_{FA}^{REQ} and MD rate P_{MD}^{REQ}.

Initialization:

Utilize the DEM and the probability models introduced in Section II to calculate the prior probabilities ($P_{k,O}^m$, $P_{k,F|O}^m$ and $P_{k,N|O}^m$) of potential statuses of each SP according to parameters $\mathbf{w}_k$, h_B, $\mathbf{u}_m$ and h_U^m;

Event Classification:

Divide all possible events in positioning process into G observation events according to the visibility of each SP, and further subdivided each of them into one normal event and Q_g failure events according to SP's status; (23), (28);

Calculate the prior probability of each observation event (P_g^m), normal event ($P_{g,0}^m$) and failure event ($P_{g,q}^m$) based on $P_{k,O}^m$, $P_{k,F|O}^m$ and $P_{k,N|O}^m$; (25), (27) and (30);

Requirement Allocation:

Allocate the overall tolerable FA rate P_{FA}^{REQ} among observation events with the scheme described in ***Algorithm 2***, and determine the threshold T_g in each event $\mathbf{o}_g$;

Allocate the overall tolerable MD rate P_{MD}^{REQ} among failure events and both directions (x and y) with the scheme described in ***Algorithm 3***, conditional MD rate $P_{MD|\mathbf{f}_q^g}^{REQ,x}$ for the x-direction in event $\mathbf{f}_q^g$;

Reliability Prediction:

for $m = 1$ to M **do**
  for $g = 1$ to G_R **do**
    for $q = 1$ to Q_g **do**
      Calculate the minimum detectable errors in x- and y-directions ($\eta_{g,q}^{*m,x}$ and $\eta_{g,q}^{*m,y}$) based on T_g, $P_{MD|\mathbf{f}_q^g}^{REQ,x}$ and $P_{MD|\mathbf{f}_q^g}^{REQ,y}$; (46)-(48);
    end for
  end for
end for

Take $\eta^* = \max\limits_{m\in\mathcal{M}}\left\{\max\limits_{g\in\mathcal{G}}\left\{\max\limits_{q\in\mathcal{Q}_g}\left\{\eta_{g,q}^{*m,x}, \eta_{g,q}^{*m,y}\right\}\right\}\right\}$ as the overall reliability prediction results; (49)-(52);

Output: η^*.

Algorithm 2 False Alarm (FA) Rate Allocation Scheme

Input: Number of observation events G, prior probability of the normal event in each observation event ($P_{g,0}^m$), overall tolerable FA rate P_{FA}^{REQ}.

Allocation:

Exclude $G_{SU}+G_{PO}$ observation events in which failure detection is unimplementable, and subtract their FA rates $P_{FA,PO}^m$ from overall tolerable FA rate P_{FA}^{REQ}; (34);

Sort the remaining $G_R = G - G_{SU} - G_{PO}$ observation events in ascending order of $P_{g,0}^m$, and find the first $g^* - 1$ events with negligible FA rates, exclude them and subtract their FA rates $P_{FA,EXL}^{REQ}$ from $P_{FA} - P_{FA,PO}^m$; (35)-(38);

Allocate $P_{FA} - P_{FA,PO}^m - P_{FA,EXL}^{REQ}$ to the remaining $G_R - g^* + 1$ observation events according to $P_{g,0}^m$; (39);

Determine the threshold T_g in each observation event $\mathbf{o}_g$ based on the allocated conditional FA rate $P_{FA|\mathbf{o}_g}^{REQ}$; (32);

Output: $P_{FA|\mathbf{o}_g}^{REQ}$ and T_g.

Algorithm 3 Missed Detection (MD) Rate Allocation Scheme

Input: Number of failure events in each observation event (Q_g), prior probability of each observation event (P_g^m) and failure event ($P_{g,q}^m$), overall tolerable MD rate P_{MD}^{REQ}.

Allocation:

Allocate P_{MD}^{REQ} to the remaining $G_R - g^* + 1$ observation events according to $P_{g,\mathbf{f}}^m$ ($P_{g,\mathbf{f}}^m = P_g^m - P_{g,0}^m$), $P_{MD,\mathbf{o}_g}^{REQ}$ to event $\mathbf{o}_g$; (41)-(42);

for $g = g^*$ to G_R **do**

  Sort the Q_g failure events in observation event $\mathbf{o}_g$ in ascending order of $P_{g,q}^m$ and find the first $q^* - 1$ events with negligible MD rates, exclude them and subtract their MD rates $P_{MD,EXL,\mathbf{o}_g}^{REQ}$ from $P_{MD,\mathbf{o}_g}^{REQ}$; (43);

  Allocate $P_{MD,\mathbf{o}_g}^{REQ} - P_{MD,EXL,\mathbf{o}_g}^{REQ}$ to the remaining $Q_g - q^* + 1$ failure events according to $P_{g,q}^m$; (44);

  Allocate the conditional MD rate $P_{MD|\mathbf{f}_q^g}^{REQ}$ of failure event $\mathbf{f}_q^g$ equally to the x- and y-directions, $P_{MD|\mathbf{f}_q^g}^{REQ,x}$ to the x-direction; (45);

end for

Output: $P_{MD|\mathbf{f}_q^g}^{REQ,x}$ and $P_{MD|\mathbf{f}_q^g}^{REQ,y}$.

APPENDIX C
PSEUDOCODE FOR THE PROPOSED VOTING-BASED CAUSE ANALYSIS METHOD

Algorithm 4 Voting-based Method for the Cause Analysis of Hazardous Area i

Input: The set $\mathcal{M}_i$ composed of sample points in i-th hazardous area, reliability prediction results ($\eta^{*m_i,x}$ and $\eta^{*m_i,y}$) corresponding to each sample point m_i ($m_i \in \mathcal{M}_i$).

Initialization:

Initialize voting vectors: $\mathbf{v}_{H_i,U}^{*x} \leftarrow \mathbf{0}_{1\times K}$, $\mathbf{v}_{H_i,F|O}^{*x} \leftarrow \mathbf{0}_{1\times K}$, $\mathbf{v}_{H_i,U}^{*y} \leftarrow \mathbf{0}_{1\times K}$, $\mathbf{v}_{H_i,F|O}^{*y} \leftarrow \mathbf{0}_{1\times K}$;

Voting Process:

for $m_i = 1$ to M_i **do**

  Calculate the prior probabilities $P_{k,B}^{m_i}$ and $P_{k,F|O}^{m_i}$;

  Find the largest number of unavailable SPs in the remaining observation events: $\bar{U}^{*m_i} = \max_{g\in\mathcal{G}^{m_i}} \{\bar{U}_g\}$;

  Find the largest number of failure SPs in the remaining failure events: $\bar{F}^{*m_i} = \max_{g\in\mathcal{G}^{m_i}} \left\{ \max_{q\in\bar{\mathcal{Q}}_g^{m_i}} \{\bar{F}_q^g\} \right\}$;

  if $\eta^{*m_i,x} > \eta_T$ **then**

    for $k = 1$ to K **do**

      if $P_{k,B}^{m_i}$ is the largest $\bar{U}^{*m_i}$ among K SPs **then**

        $\mathbf{v}_{H_i,U}^{*x}[k] \leftarrow \mathbf{v}_{H_i,U}^{*x}[k] + \frac{(\eta^{*m_i,x}-\eta_T)^2}{\sum_{m_i\in\mathcal{M}_i}(\eta^{*m_i,x}-\eta_T)^2}$;

      end if

      if $P_{k,F|O}^{m_i}$ is the largest $\bar{F}^{*m_i}$ among K SPs **then**

        $\mathbf{v}_{H_i,F|O}^{*x}[k] \leftarrow \mathbf{v}_{H_i,F|O}^{*x}[k] + \frac{(\eta^{*m_i,x}-\eta_T)^2}{\sum_{m_i\in\mathcal{M}_i}(\eta^{*m_i,x}-\eta_T)^2}$;

      end if

    end for

  end if

  Repeat steps 6-15 in the y-direction;

end for

$\mathbf{v}_{H_i,U}^{*x} \leftarrow \langle \mathbf{v}_{H_i,U}^{*x} \rangle$, $\mathbf{v}_{H_i,F|O}^{*x} \leftarrow \left\langle \mathbf{v}_{H_i,F|O}^{*x} \right\rangle$, $\mathbf{v}_{H_i,U}^{*y} \leftarrow \left\langle \mathbf{v}_{H_i,U}^{*y} \right\rangle$, $\mathbf{v}_{H_i,F|O}^{*y} \leftarrow \left\langle \mathbf{v}_{H_i,F|O}^{*y} \right\rangle$;

Output: $\mathbf{v}_{H_i,U}^{*x}$, $\mathbf{v}_{H_i,F|O}^{*x}$, $\mathbf{v}_{H_i,F|O}^{*y}$ and $\mathbf{v}_{H_i,F|O}^{*y}$.

APPENDIX D
PROOF OF LINEAR RELATIONSHIP BETWEEN η^* AND σ_C

It can be seen from equation (48) that the value of $\eta_{g,q}^{*m,x}$ depends on the largest failure slope $s_{g,q}^{*m,x}$, the worst fault vector $\mathbf{b}_{g,q}^{*m,x}$ and matrix $(\mathbf{I} - \mathbf{H}_g\mathbf{G}_g)$. First, we investigate the relationship between matrix $(\mathbf{I} - \mathbf{H}_g\mathbf{G}_g)$ and parameter σ_C. As mentioned at the beginning of Section III.A, matrix $\mathbf{H}_g$ is obtained by normalizing the Jacobian matrix $\mathbf{H}_{g*}$ according to the covariance matrix $\mathbf{V}_* = \sigma_C^2 \cdot \mathbf{I}_N$, that is, $\mathbf{H}_g = \mathbf{V}_*^{-1/2}\mathbf{H}_{g*}$. Similarly, matrix $\mathbf{G}_g$ can be expressed as:

$$\begin{aligned}\mathbf{G}_g &= \left(\mathbf{H}_g^T\mathbf{H}_g\right)^{-1}\mathbf{H}_g^T \\ &= \left(\mathbf{H}_{g*}^T\mathbf{V}_*^{-1/2}\mathbf{V}_*^{-1/2}\mathbf{H}_{g*}\right)\mathbf{H}_{g*}^T\mathbf{V}_*^{-1/2} \\ &= \left(\mathbf{H}_{g*}^T\mathbf{H}_{g*}\right)\mathbf{H}_{g*}^T\mathbf{V}_*^{1/2} = \mathbf{G}_{g*}\mathbf{V}_*^{1/2},\end{aligned} \tag{65}$$

where $\mathbf{G}_{g*} = \left(\mathbf{H}_{g*}^T\mathbf{H}_{g*}\right)\mathbf{H}_{g*}^T$. Then, we can get the following relationship:

$$\begin{aligned}\mathbf{H}_g\mathbf{G}_g &= \mathbf{V}_*^{-1/2}\mathbf{H}_{g*}\left(\mathbf{H}_{g*}^T\mathbf{H}_{g*}\right)\mathbf{H}_{g*}^T\mathbf{V}_*^{1/2} \\ &= \mathbf{H}_{g*}\left(\mathbf{H}_{g*}^T\mathbf{H}_{g*}\right)\mathbf{H}_{g*}^T = \mathbf{H}_{g*}\mathbf{G}_{g*}.\end{aligned} \tag{66}$$

Since matrix $\mathbf{H}_{g*}$ is only determined by the geometry of anchor nodes, it can be concluded that matrix $(\mathbf{I} - \mathbf{H}_g\mathbf{G}_g)$ will not change with parameter σ_C.

Moreover, as can be seen from equation (26), the decision threshold T_g is independent of parameter σ_C. Thus, according to equation (46), the worst fault vector $\mathbf{b}_{g,q}^{*m,x}$ remains unchanged with the change of σ_C.

To investigate the relationship between $s_{g,q}^{*m,x}$ and σ_C, we rewrite equation (47) as

$$\begin{aligned}s &\triangleq \frac{\mathbf{b}^T\mathbf{s}_x\mathbf{s}_x^T\mathbf{b}}{\mathbf{b}^T(\mathbf{I}-\mathbf{H}\mathbf{G})\mathbf{b}^T} = \frac{\mathbf{b}^T\mathbf{G}^T\boldsymbol{\alpha}_x\boldsymbol{\alpha}_x^T\mathbf{G}\mathbf{b}}{\mathbf{b}^T(\mathbf{I}-\mathbf{H}\mathbf{G})\mathbf{b}^T} \\ &= \frac{\mathbf{b}^T\mathbf{G}_*^T\boldsymbol{\alpha}_x\boldsymbol{\alpha}_x^T\mathbf{G}_*\mathbf{b}}{\mathbf{b}^T(\mathbf{I}-\mathbf{H}_*\mathbf{G}_*)\mathbf{b}^T}\cdot\sigma_C^2.\end{aligned} \tag{67}$$

It can be seen from the above equation that the value of failure slope s is linear with σ_C^2. In addition, as mentioned above, the worst fault vector $\mathbf{b}_{g,q}^{*m,x}$ is independent of σ_C. Therefore, the value of the largest failure slope $s_{g,q}^{*m,x}$ is also linear with σ_C^2.

According to the above analysis, vector $\mathbf{b}_{g,q}^{*m,x}$ and matrix $(\mathbf{I} - \mathbf{H}_g\mathbf{G}_g)$ are both independent of σ_C, while $s_{g,q}^{*m,x}$ is linear with σ_C^2. Then, it is easy to draw the conclusion from equation (48) that $\eta_{g,q}^{*m,x}$ has a linear relationship with parameter σ_C. Finally, since η^* represents the largest $\eta_{g,q}^{*m,x}$ in all possible failure events and sample points, it also has a linear relationship with σ_C.

REFERENCES

[1] A. Küpper, *Location-based services: fundamentals and operation*. John Wiley & Sons, 2005.

[2] A. Hoglund, X. Lin, O. Liberg, A. Behravan, E. A. Yavuz, M. Van Der Zee, Y. Sui, T. Tirronen, A. Ratilainen, and D. Eriksson, "Overview of 3GPP release 14 enhanced NB-IoT," *IEEE Network*, vol. 31, no. 6, pp. 16–22, 2017.

[3] 3GPP TR 38.855, "Study on NR positioning support," Rel. 16, 2019.

[4] J. Lee, E. Tejedor, K. Ranta-aho, H. Wang, K. Lee, E. Semaan, E. Mohyeldin, J. Song, C. Bergljung, and S. Jung, "Spectrum for 5G: Global status, challenges, and enabling technologies," *IEEE Communications Magazine*, vol. 56, no. 3, pp. 12–18, 2018.

[5] T. O. Olasupo, "Wireless communication modeling for the deployment of tiny IoT devices in rocky and mountainous environments," *IEEE Sensors Letters*, vol. 3, no. 7, pp. 1–4, 2019.

[6] X. Zhang, X. Tao, F. Zhu, X. Shi, and F. Wang, "Quality assessment of GNSS observations from an android N smartphone and positioning performance analysis using time-differenced filtering approach," *GPS Solutions*, vol. 22, no. 3, 2018.

[7] S. Fischer, "Observed time difference of arrival (OTDOA) positioning in 3GPP LTE," *Qualcomm White Pap*, 2014.

[8] K. Shamaei and Z. M. Kassas, "LTE receiver design and multipath analysis for navigation in urban environments," *Navigation*, vol. 65, no. 4, pp. 655–675, 2018.

[9] M. Driusso, C. Marshall, M. Sabathy, F. Knutti, H. Mathis, and F. Babich, "Indoor positioning using LTE signals," in *2016 International Conference on Indoor Positioning and Indoor Navigation (IPIN)*, 2016, pp. 1–8.

[10] L. Peraza, M. Semmling, C. Falck, O. Pavlova, S. Gerland, and J. Wickert, "Analysis of grazing GNSS reflections observed at the zeppelin mountain station, spitsbergen," *Radio Science*, vol. 52, no. 11, pp. 1352–1362, 2017.

[11] W. Jiang, D. Liu, B. Cai, C. Rizos, J. Wang, and W. Shangguan, "A fault-tolerant tightly coupled GNSS/INS/OVS integration vehicle navigation system based on an FDP algorithm," *IEEE Transactions on Vehicular Technology*, vol. 68, no. 7, pp. 6365–6378, 2019.

[12] R. Rahdar, J. T. Stracener, and E. V. Olinick, "A systems engineering approach to improving the accuracy of mobile station location estimation," *IEEE Systems Journal*, vol. 8, no. 1, pp. 14–22, 2014.

[13] D. Lu, S. Jiang, B. Cai, W. Shangguan, X. Liu, and J. Luan, "Quantitative analysis of GNSS performance under railway obstruction environment," in *2018 IEEE/ION Position, Location and Navigation Symposium (PLANS)*, 2018, pp. 1074–1080.

[14] Q. Liu, R. Liu, Z. Wang, and Y. Zhang, "Simulation and analysis of device positioning in 5G ultra-dense network," in *2019 15th International Wireless Communications & Mobile Computing Conference (IWCMC)*, 2019, pp. 1529–1533.

[15] K. Shamaei and Z. M. Kassas, "LTE multipath mitigation for positioning in urban environments," *Navigation: Journal of the Institute of Navigation*, 2017.

[16] G. Ding, Q. Wu, L. Zhang, Y. Lin, T. A. Tsiftsis, and Y. Yao, "An amateur drone surveillance system based on the cognitive internet of things," *IEEE Communications Magazine*, vol. 56, no. 1, pp. 29–35, 2018.

[17] Z. Xue, J. Wang, G. Ding, Q. Wu, Y. Lin, and T. A. Tsiftsis, "Device-to-device communications underlying UAV-supported social networking," *IEEE Access*, vol. 6, pp. 34 488–34 502, 2018.

[18] J. Sun, W. Wang, L. Kou, Y. Lin, L. Zhang, Q. Da, and L. Chen, "A data authentication scheme for UAV ad hoc network communication," *The Journal of Supercomputing*, vol. 76, no. 6, pp. 4041–4056, 2020.

[19] Y. Lin, M. Wang, X. Zhou, G. Ding, and S. Mao, "Dynamic spectrum interaction of UAV flight formation communication with priority: A deep reinforcement learning approach," *IEEE Transactions on Cognitive Communications and Networking*, vol. 6, no. 3, pp. 892–903, 2020.

[20] L. Chaves, I. V. Bessa, H. Ismail, A. B. dos Santos Frutuoso, L. Cordeiro, and E. B. de Lima Filho, "Dsverifier-aided verification applied to attitude control software in unmanned aerial vehicles," *IEEE Transactions on Reliability*, vol. 67, no. 4, pp. 1420–1441, 2018.

[21] M. Noor-A-Rahim, M. O. Khyam, G. G. M. N. Ali, Z. Liu, D. Pesch, and P. H. J. Chong, "Reliable state estimation of an unmanned aerial vehicle over a distributed wireless iot network," *IEEE Transactions on Reliability*, vol. 68, no. 3, pp. 1061–1069, 2019.

[22] T. Wang, Z. Zheng, Y. Lin, S. Yao, and X. Xie, "Reliable and robust unmanned aerial vehicle wireless video transmission," *IEEE Transactions on Reliability*, vol. 68, no. 3, pp. 1050–1060, 2019.

[23] Z. Liu, Z. Li, B. Liu, X. Fu, I. Raptis, and K. Ren, "Rise of mini-drones: Applications and issues," in *2015 Workshop on Privacy-Aware Mobile Computing (PAMCO '15)*, 2015, pp. 7–12.

[24] S. Zhang, Y. Zeng, and R. Zhang, "Cellular-enabled UAV communication: A connectivity-constrained trajectory optimization perspective," *IEEE Transactions on Communications*, vol. 67, no. 3, pp. 2580–2604, 2019.

[25] Z. Wang, R. Liu, Q. Liu, J. S. Thompson, and M. Kadoch, "Energy-efficient data collection and device positioning in UAV-assisted IoT," *IEEE Internet of Things Journal*, vol. 7, no. 2, pp. 1122–1139, 2020.

[26] C. Ou and K. Ssu, "Sensor position determination with flying anchors in three-dimensional wireless sensor networks," *IEEE Transactions on Mobile Computing*, vol. 7, no. 9, pp. 1084–1097, 2008.

[27] G. Han, J. Jiang, C. Zhang, T. Q. Duong, M. Guizani, and G. K. Karagiannidis, "A survey on mobile anchor node assisted localization in wireless sensor networks," *IEEE Communications Surveys & Tutorials*, vol. 18, no. 3, pp. 2220–2243, 2016.

[28] Z. Liu, Y. Chen, B. Liu, C. Cao, and X. Fu, "HAWK: An unmanned mini-helicopter-based aerial wireless kit for localization," *IEEE Transactions on Mobile Computing*, vol. 13, no. 2, pp. 287–298, 2014.

[29] A. Wang, X. Ji, D. Wu, X. Bai, N. Ding, J. Pang, S. Chen, X. Chen, and D. Fang, "GuideLoc: UAV-assisted multitarget localization system for disaster rescue," *Mobile Information Systems*, vol. 2017, 2017.

[30] H. Sallouha, M. M. Azari, A. Chiumento, and S. Pollin, "Aerial anchors positioning for reliable RSS-based outdoor localization in urban environments," *IEEE Wireless Communications Letters*, vol. 7, no. 3, pp. 376–379, 2018.

[31] H. Sallouha, M. M. Azari, and S. Pollin, "Energy-constrained UAV trajectory design for ground node localization," in *2018 IEEE Global Communications Conference (GLOBECOM)*, 2018, pp. 1–7.

[32] R. G. Brown, "Receiver autonomous integrity monitoring," *Global positioning system: theory and applications*, vol. 2, pp. 143–165, 2003.

[33] R. G. Brown and P. W. Mcburney, "Self-contained GPS integrity check using maximum solution separation," *NAVIGATION*, vol. 35, no. 1, pp. 41–53, 1988.

[34] M. Joerger, F. Chan, and B. Pervan, "Solution separation versus residual-based RAIM," *NAVIGATION*, vol. 61, no. 4, pp. 273–291, 2014.

[35] J. Blanch, A. Ene, T. Walter, and P. Enge, "An optimized multiple hypothesis RAIM algorithm for vertical guidance," in *Proceedings of the 20th International Technical Meeting of the Satellite Division of The Institute of Navigation (ION GNSS 2007)*, 2007, pp. 2924–2933.

[36] N. Zhu, J. Marais, D. Btaille, and M. Berbineau, "GNSS position integrity in urban environments: A review of literature," *IEEE Transactions on Intelligent Transportation Systems*, vol. 19, no. 9, pp. 2762–2778, 2018.

[37] F. C. Meng, S. Wang, and B. C. Zhu, "Satellite selection and RAIM for GNSS reliability enhancement in multi-constellation," in *Proceedings of the 2014 International Technical Meeting of The Institute of Navigation*, 2014, pp. 78–88.

[38] F. Meng, S. Wang, and B. Zhu, "GNSS reliability and positioning accuracy enhancement based on fast satellite selection algorithm and RAIM in multiconstellation," *IEEE Aerospace and Electronic Systems Magazine*, vol. 30, no. 10, pp. 14–27, 2015.

[39] T. Murphy and T. Imrich, "Implementation and operational use of ground-based augmentation systems (GBASs)ła component of the future air traffic management system," *Proceedings of the IEEE*, vol. 96, no. 12, pp. 1936–1957, 2008.

[40] S. Pullen, M. Luo, S. Gleason, G. Xie, J. Lee, D. Akos, P. Enge, and B. Pervan, "GBAS validation methodology and test results from the stanford LAAS integrity monitor testbed," in *Proceedings of the 13th International Technical Meeting of the Satellite Division of The Institute of Navigation (ION GPS 2000)*, 2000, pp. 1191–1201.

[41] M. Siergiejczyk, A. Rosiński, and K. Krzykowska, "Reliability assessment of supporting satellite system EGNOS," in *New Results in Dependability and Computer Systems*. Springer, 2013, pp. 353–363.

[42] H. Habereder, T. Schempp, and M. Bailey, "Performance enhancements for the next phase of WAAS," in *Proceedings of the 17th International Technical Meeting of the Satellite Division of The Institute of Navigation (ION GNSS 2004)*, 2004, pp. 1350–1358.

[43] A. Macwan, G. Nejat, and B. Benhabib, "Target-motion prediction for robotic search and rescue in wilderness environments," *IEEE Transactions on Systems, Man, and Cybernetics, Part B (Cybernetics)*, vol. 41, no. 5, pp. 1287–1298, 2011.

[44] X. Shi, G. Mao, Z. Yang, and J. Chen, "Localization algorithm design and performance analysis in probabilistic LOS/NLOS environment," in *2016 IEEE International Conference on Communications (ICC)*, 2016, pp. 1–6.

[45] A. Conti, S. Mazuelas, S. Bartoletti, W. C. Lindsey, and M. Z. Win, "Soft information for localization-of-things," *Proceedings of the IEEE*, vol. 107, no. 11, pp. 2240–2264, 2019.
[46] P. Wang and Y. J. Morton, "Multipath estimating delay lock loop for LTE signal TOA estimation in indoor and urban environments," *IEEE Transactions on Wireless Communications*, vol. 19, no. 8, pp. 5518–5530, 2020.
[47] 3GPP TR 38.901, "Study on channel model for frequencies from 0.5 to 100 GHz," Rel. 16, 2019.
[48] A. Al-Hourani, S. Kandeepan, and S. Lardner, "Optimal LAP altitude for maximum coverage," *IEEE Wireless Communications Letters*, vol. 3, no. 6, pp. 569–572, 2014.
[49] D. Kidner, M. Dorey, and D. Smith, "What's the point? Interpolation and extrapolation with a regular grid DEM," in *Fourth International Conference on GeoComputation, Fredericksburg, VA, USA*, 1999.
[50] I. G. Hannah and E. P. Kontar, "Differential emission measures from the regularized inversion of Hinode and SDO data," *Astronomy & Astrophysics*, vol. 539, p. A146, 2012.
[51] S. P. Wechsler, "Uncertainties associated with digital elevation models for hydrologic applications: a review," *Hydrology and Earth System Sciences*, vol. 11, no. 4, pp. 1481–1500, 2007.
[52] S. Frattasi and F. Della Rosa, *Mobile positioning and tracking: from conventional to cooperative techniques*. John Wiley & Sons, 2017.
[53] M. Joerger and B. Pervan, "Kalman filter-based integrity monitoring against sensor faults," *Journal of Guidance, Control, and Dynamics*, vol. 36, no. 2, pp. 349–361, 2013.
[54] C. L. Sang, M. Adams, T. Hörmann, M. Hesse, M. Porrmann, and U. Rckert, "An analytical study of time of flight error estimation in two-way ranging methods," in *2018 International Conference on Indoor Positioning and Indoor Navigation (IPIN)*, 2018, pp. 1–8.
[55] "Part 15.4: Wireless medium access control (MAC) and physical layer (PHY) specifications for low-rate wireless personal area networks (WPANs): Amendment 1: Add alternate PHYs," *IEEE Std 802.15.4a-2007 (Amendment to IEEE Std 802.15.4-2006)*, pp. 1–210, 2007.
[56] E. Akyol, K. Viswanatha, and K. Rose, "On conditions for linearity of optimal estimation," *IEEE Transactions on Information Theory*, vol. 58, no. 6, pp. 3497–3508, 2012.

Zijie Wang received the B.S. degree in electrical and information engineering from Beihang University in 2017. He is currently pursuing the Ph.D. degree with the School of Electronic and Information Engineering, Beihang University, China. His current research interests include global navigation satellite system, terrestrial localization systems, indoor/outdoor seamless positioning, unmanned aerial vehicles, as well as the applications of these technologies to 5G and Internet of Things networks.

Rongke Liu (SM'19) received the B.S. and Ph.D. degrees from Beihang University in 1996 and 2002, respectively. He was a Visiting Professor with the Florida Institution of Technology, USA, in 2005; The University of Tokyo, Japan, in 2015; and the University of Edinburgh, U.K., in 2018, respectively. He is currently a Full Professor with the School of Electronic and Information Engineering, Beihang University. He received the support of the New Century Excellent Talents Program from the Minister of Education, China. He has attended many special programs, such as China Terrestrial Digital Broadcast Standard. He has published over 100 papers in international conferences and journals. He has been granted 20 patents. His research interest covers wireless multimedia communication, compression coding, channel coding, and aerospace communication.

Qirui Liu received the B.S. degree in communication engineering from the School of Computer and Communication Engineering, University of Science and Technology Beijing (USTB) in 2019. He is currently pursuing the Ph.D. degree with the School of Electronic and Information Engineering, Beihang University, China. His current research interests include global navigation satellite system, localization techniques, indoor positioning and navigation, and the applications of these technologies to 5G and Internet of Things networks.

Lincong Han received the B.S. degree in communication engineering from Shandong University (SDU), China, in 2017. She is currently pursuing the Ph.D. degree with the School of Electronic and Information Engineering, Beihang University, China. Her current research interests include 5G positioning, wireless communication, non-orthogonal multiple access (NOMA) and Internet of Things networks.

John S. Thompson (F'16) is currently a Professor at the School of Engineering in the University of Edinburgh. He specializes in antenna array processing, cooperative communications systems, energy efficient wireless communications and their applications. He has published in excess of three hundred and fifty papers on these topics. In 2018, he was the co-chair of the IEEE Smartgridcomm conference held in Aalborg, Denmark. He currently participates in two UK research projects which study new concepts for signal processing and for next generation wireless communications. In January 2016, he was elevated to Fellow of the IEEE for contributions to antenna arrays and multi-hop communications. In 2015-2018, he has been recognised by Thomson Reuters as a highly cited researcher.

Yun Lin received the B.S. degree from Dalian Maritime University, Dalian, China, in 2003, the M.S. degree from the Harbin Institute of Technology, Harbin, China, in 2005, and the Ph.D. degree from Harbin Engineering University, Harbin, China, in 2010. From 2014 to 2015, he was a Research Scholar with Wright State University, Dayton, OH, USA. He is currently a Full Professor with the College of Information and Communication Engineering, Harbin Engineering University, Harbin, China. He has authored or coauthored more than 150 international peer-reviewed journal or conference papers. He has four high-cited papers and several best conference papers. His current research interests include machine learning and data analytics over wireless networks, signal processing and analysis, cognitive radio and software defined radio, artificial intelligence, and pattern recognition.

Weiqing Mu received Ph.D. degree in Communication and Information Engineering from Beihang University, in 2018. He is now working in Postdoctoral Workstation of China Research Institute of Radiowave Propagation. His current research interests include spectrum monitoring, dynamic frequency sharing, and RF relative measurement.